



This is a repository copy of *Current Understanding of Structure–Processing–Property Relationships in BaTiO<sub>3</sub>–Bi(M)O<sub>3</sub> Dielectrics*.

White Rose Research Online URL for this paper:  
<http://eprints.whiterose.ac.uk/107980/>

Version: Accepted Version

---

**Article:**

Beuerlein, M.A., Kumar, N., Usher, T.M. et al. (7 more authors) (2016) Current Understanding of Structure–Processing–Property Relationships in BaTiO<sub>3</sub>–Bi(M)O<sub>3</sub> Dielectrics. *Journal of the American Ceramic Society*, 99 (9). pp. 2849-2870. ISSN 0002-7820

<https://doi.org/10.1111/jace.14472>

---

This is the peer reviewed version of the following article: Beuerlein, M. A., Kumar, N., Usher, T. M., Brown-Shaklee, H. J., Raengthon, N., Reaney, I. M., ... & Brennecka, G. L. (2016). Current Understanding of Structure–Processing–Property Relationships in BaTiO<sub>3</sub>–Bi (M) O<sub>3</sub> Dielectrics. *Journal of the American Ceramic Society*, which has been published in final form at <http://doi.org/10.1111/jace.14472>. This article may be used for non-commercial purposes in accordance with Wiley Terms and Conditions for Self-Archiving.

**Reuse**

Unless indicated otherwise, fulltext items are protected by copyright with all rights reserved. The copyright exception in section 29 of the Copyright, Designs and Patents Act 1988 allows the making of a single copy solely for the purpose of non-commercial research or private study within the limits of fair dealing. The publisher or other rights-holder may allow further reproduction and re-use of this version - refer to the White Rose Research Online record for this item. Where records identify the publisher as the copyright holder, users can verify any specific terms of use on the publisher's website.

**Takedown**

If you consider content in White Rose Research Online to be in breach of UK law, please notify us by emailing [eprints@whiterose.ac.uk](mailto:eprints@whiterose.ac.uk) including the URL of the record and the reason for the withdrawal request.



[eprints@whiterose.ac.uk](mailto:eprints@whiterose.ac.uk)  
<https://eprints.whiterose.ac.uk/>

**Current Understanding of Structure-Processing-Property Relationships in BaTiO<sub>3</sub>-  
Bi(M)O<sub>3</sub> Dielectrics**

Michaela A. Beuerlein<sup>1</sup>, Nitish Kumar<sup>2</sup>, Tedi-Marie Usher<sup>3\*</sup>, Harlan James  
Brown-Shaklee<sup>4</sup>, Natthaphon Raengthon<sup>5</sup>, Ian M. Reaney<sup>6</sup>, David P. Cann<sup>2</sup>, Jacob L.  
Jones<sup>3</sup>, and Geoff L. Brenneka<sup>1†</sup>

<sup>1</sup>Department of Metallurgical and Materials Engineering, Colorado School of  
Mines, Golden, CO 80401

<sup>2</sup>Materials Science, School of Mechanical, Industrial, and Manufacturing  
Engineering, Oregon State University, Corvallis, OR 97331

<sup>3</sup>Department of Materials Science and Engineering, North Carolina State  
University, Raleigh, NC 27695

<sup>4</sup>Electronic, Optical, and Nanostructured Materials Department, Sandia National  
Laboratories, Albuquerque, NM 87185

<sup>5</sup>Department of Materials Science, Faculty of Science, Chulalongkorn University,  
Bangkok 10330, Thailand

<sup>6</sup>Department of Engineering Materials, University of Sheffield, Sheffield, United  
Kingdom

\*Current affiliation: Chemical and Engineering Materials Division, Oak Ridge National  
Laboratory, Oak Ridge, TN 37831

†Author to whom correspondence should be addressed. email: gbrennec@mines.edu

## **Abstract**

As part of a continued push for high permittivity dielectrics suitable for use at elevated operating temperatures and/or large electric fields, modifications of  $\text{BaTiO}_3$  with  $\text{Bi(M)O}_3$ , where M represents a net-trivalent B-site occupied by one or more species, have received a great deal of recent attention. Materials in this composition family exhibit weakly-coupled relaxor behavior that is not only remarkably stable at high temperatures and under large electric fields, but is also quite similar across various identities of M. Moderate levels of Bi content (as much as 50 mol%) appear to be crucial to the stability of the dielectric response. In addition, the presence of significant Bi reduces the processing temperatures required for densification and increases the required oxygen content in processing atmospheres relative to traditional X7R-type  $\text{BaTiO}_3$ -based dielectrics. Although detailed understanding of the structure-processing-property relationships in this class of materials is still in its infancy, this article reviews the current state of understanding of the mechanisms underlying the high and stable values of both relative permittivity and resistivity that are characteristic of  $\text{BaTiO}_3$ - $\text{Bi(M)O}_3$  dielectrics as well as the processing challenges and opportunities associated with these materials.

## **Introduction**

In the continual quest for increased integration, efficiency, and process monitoring, electronics systems are being subjected to increasingly harsh operating conditions. One key class of components that has received a great deal of attention over the past decade is capacitors that can operate efficiently and reliably under large fields and at temperatures  $\geq 200$  °C.<sup>1-4</sup> For example, devices built around wide bandgap

semiconductors such as SiC and GaN can operate with greater efficiency, higher frequencies, and higher powers than their Si-based counterparts, but even these more efficient devices dissipate sufficient heat that active cooling is often required in order to accommodate the operating temperature limitations of nearby passive components such as capacitors. Such temperature concerns are only exacerbated with passive components for which high power operation in the 10s of kHz frequency regime results in non-negligible self-heating. Thus, low-loss ceramic capacitors with low equivalent series resistance (ESR) capable of operating reliably at temperatures of 200 °C and above are of great interest.

BaTiO<sub>3</sub>-based compositions remain the workhorses of high permittivity ceramic capacitors, but as maximum rating temperatures have crept from 125 °C of the X7R specification to 150 °C (X8R), and 200 °C (X9R) or above, manufacturers have been forced to abandon traditional approaches to engineering temperature stability. The wildly successful approach of using core-shell dopant profiles to smear out spatially-graded phase transitions and associated permittivity maxima is insufficient for operating temperatures substantially above the Curie Temperature ( $T_C$ , the temperature at which the transition between a cubic phase above  $T_C$  and a non-cubic phase below  $T_C$  is accompanied by a large maximum in relative permittivity;  $T_C$  for BaTiO<sub>3</sub> is approximately 125 °C). While the solid solution of BaTiO<sub>3</sub> and PbTiO<sub>3</sub> seems to provide a simple method for shifting the temperature maxima to higher values, both the difficulty of cofiring Pb-based materials with low-cost Ni electrodes and the parallel push to eliminate Pb from such compositions for environmental and health concerns further complicate the situation. At present, three types of dielectric materials seem poised as

potential candidates to lead the push above 200 °C operating temperatures: linear dielectrics such as CaZrO<sub>3</sub> and alkali-free glasses,<sup>5-8</sup> Pb-free normal ferroelectrics (potentially mixed with antiferroelectric compounds) that exhibit higher T<sub>C</sub> values than BaTiO<sub>3</sub>,<sup>9-14</sup> and a recently-developed class of weakly-coupled relaxor dielectrics based on Bi(M)O<sub>3</sub> additions to normal ferroelectrics.<sup>15-19</sup> Other reports have summarized the performance of these various classes of materials;<sup>3, 4, 20</sup> the current work examines the structure and processing origins of the rather unusual properties of the last category, with a particular focus on BaTiO<sub>3</sub>-Bi(M)O<sub>3</sub> materials, where M represents one or more trivalent cations able to occupy the perovskite B-site (e.g., M = Fe, Sc, In, Ga, Al, ...) or a stoichiometric ratio of non-trivalent cations that average out to a trivalent equivalent (e.g., M = Zn<sub>1/2</sub>Ti<sub>1/2</sub>, Mg<sub>2/3</sub>Nb<sub>1/3</sub>, ...). In order to appropriately frame the weakly-coupled relaxor dielectric response of these materials, we compare their behavior to traditional ferroelectric and prototypic relaxor behavior.

Ever since its discovery, BaTiO<sub>3</sub> has been one of the most widely studied ferroelectric materials, and it remains the cornerstone of the capacitor industry today. The BaTiO<sub>3</sub> crystal is stable as a cubic perovskite (Pm $\bar{3}$ m) above T<sub>C</sub> (~130 °C) and follows the Curie-Weiss law

$$\epsilon_r = \frac{C}{T-T_C} \quad (1)$$

where  $\epsilon_r$  is relative permittivity, C is the Curie constant, T is the measurement temperature, and T<sub>C</sub> is the Curie temperature. With further decreases in temperature, BaTiO<sub>3</sub> transforms from tetragonal symmetry (P4mm) to orthorhombic symmetry (Amm2) at ~ 5 °C and finally to rhombohedral symmetry (R3m) at ~ -90 °C. Each of

these phase transitions is associated with a frequency-independent anomaly in dielectric constant (Figure 1(a)). On making chemical substitutions onto the A- or B-site, a crossover to a relaxor state often occurs, depending upon the type and mole fraction of the substitution. In general, after substitution, these transition temperatures shift and become broad, leading to a diffuse phase transition (DPT). A DPT is different from a first order transition in normal ferroelectrics, as it starts to show deviation from the Curie-Weiss law at temperatures above  $T_{max}$  (Figure 1(b)). It does not, however, exhibit the frequency dispersion at the permittivity maximum which is characteristic of relaxor materials. Close to the dielectric maximum, the permittivity ( $\epsilon'$ ) can be described by the following equation as suggested by Santos et al.<sup>21</sup> (one of the several functions proposed in literature),

$$\epsilon' = \frac{\epsilon'_{max}}{1 + \left(\frac{T - T_{max}}{\delta}\right)^\gamma} \quad (2)$$

where,  $\epsilon'_{max}$  is maximum permittivity,  $\delta$  describes the degree of diffuseness (a parameterized description of the temperature breadth of a phase transition), and  $\gamma$  describes the type of transition which increases with the increase in mole fraction of chemical substitution from a value of 1 for a normal ferroelectric towards 2 for a complete DPT. At even higher levels of substitution, the solid solution becomes a relaxor with a characteristic frequency-dispersion at the dielectric maxima (Figure 1(c)), and follows the Vogel-Fulcher law<sup>22, 23</sup> in general:

$$f = f_0 \exp\left(\frac{E_a}{k(T_{max} - T_f)}\right) \quad (3)$$

where  $f$  is the measurement frequency,  $f_0$  is a fitting parameter,  $k$  is the Boltzmann constant, and  $E_a$  is activation energy. In  $\text{BaTiO}_3\text{-Bi}(\text{Zn}_{1/2}\text{Ti}_{1/2})\text{O}_3$  (BT-BZT) ceramics, for

example, this crossover from normal ferroelectric to relaxor takes place around 8 mol% BZT. For isovalent substitutions, the mole fraction of substitutions required may be higher, as they are expected to create relatively less disorder than aliovalent cations.<sup>24</sup> The type of substitution not only determines the degree of crossover to relaxor behavior, it also regulates technologically important material properties like the temperature coefficient of permittivity ( $TC\varepsilon = \frac{1}{\varepsilon} \frac{\partial \varepsilon}{\partial T}$ ).<sup>25</sup> For BT- Bi(M)O<sub>3</sub> ceramics in general, it has been found that as the amount of substitution (Bi<sup>3+</sup> for Ba<sup>2+</sup> and M<sup>3+</sup> for Ti<sup>4+</sup>) increases, the permittivity becomes more stable with temperature and the absolute value of TCε decreases, which can be further manipulated by introducing ternary or quaternary perovskite end-members to the solid solutions.<sup>3, 25-27</sup>

Typical ferroelectric materials, such as BaTiO<sub>3</sub> and Pb(Zr<sub>x</sub>Ti<sub>1-x</sub>)O<sub>3</sub> (for  $x \lesssim 0.95$ , BT and PZT, respectively), are characterized by a sharp peak in relative permittivity ( $\varepsilon_r$ , often on the order of  $\sim 10$ - $15,000$ <sup>28</sup>) associated with  $T_C$ . Above  $T_C$ , the permittivity follows the Curie-Weiss Law (Equation 1).

In certain cases, the compositional and site disorder that accompanies solid solutions produces an  $\varepsilon(T)$  relationship that deviates from Curie-Weiss behavior above  $T_c$  and produces a broad frequency-dependent  $\varepsilon(T)$  curve that is characteristic of relaxor dielectrics.<sup>20, 29, 30</sup> Research on relaxor behavior was first reported in BaTiO<sub>3</sub>-BaSnO<sub>3</sub> in 1954 by Smolenskii et al. along with early reports on Bi-based relaxors,<sup>31</sup> but the majority of research on relaxor materials has focused on Pb-based solid solutions. The earliest studies of relaxor materials focused on chemical disorder on the perovskite B-site (e.g., Ba(Ti,Sn)O<sub>3</sub>, Pb(Mg<sub>1/3</sub>,Nb<sub>2/3</sub>)O<sub>3</sub>, K(Ta,Nb)O<sub>3</sub>) with essentially the same physics

successfully applied to materials with A-site disorder, such as  $(\text{Pb,Lu})(\text{Zr,Ti})\text{O}_3$ .<sup>30, 32</sup> These studies invoked the concept of polar nano-regions (PNRs), which are nanoscale regions of polarization within a non-polar matrix in order to explain the frequency-dependence.<sup>20, 33-35</sup> Recent interest in the development of Pb-free dielectrics has led to the discovery of a new family of materials that have been classified as weakly-coupled relaxors. The frequency- and temperature-dependent dielectric response of these materials can be described by the Curie-Weiss and PNR model applied to traditional relaxors, but Vogel-Fulcher analysis reveals activation energies that are roughly an order of magnitude higher than in traditional relaxors, related to the unusual (and desirable) temperature stability of permittivity above  $T_{\text{max}}$ .<sup>36</sup> Figure 2 provides an example of relative permittivity as a function of temperature for  $0.50\text{BaTiO}_3\text{-}0.25\text{Bi}(\text{Zn}_{1/2}\text{Ti}_{1/2})\text{O}_3\text{-}0.25\text{BiScO}_3$  (0.5BT-0.25BZT-0.25BS) and demonstrates the significant difference in low-field permittivity of these materials compared to that of prototypic normal ferroelectrics ( $\text{BaTiO}_3$ ) and relaxors ( $\text{Pb}(\text{Mg}_{1/3}\text{Nb}_{2/3})\text{O}_3$ , PMN), shown in the inset. In addition to temperature stability, materials in this BT-Bi(M)O<sub>3</sub> family of weakly coupled relaxors also frequently exhibit attractive stability under large electric fields (Figure 3). While permittivity values for BT-Bi(M)O<sub>3</sub> materials start lower than many traditional optimized BaTiO<sub>3</sub>-based capacitor compositions, tuning is much less severe in these materials, such that at high fields they tend to maintain higher permittivity values than other known materials. Furthermore, both the resistivity and activation energy for charge transport in BT-Bi(M)O<sub>3</sub> materials tend to be noticeably larger than values seen even in highly-engineered commercial compositions (Figure 4). This is particularly important because it implies that these materials could be significantly more reliable when operated at the high



fields and elevated temperatures at which their properties exceed those of traditional high-permittivity materials. Intriguingly, the measured activation energies for these materials are commonly approximately half of the optical band gap, characteristic of conduction dominated by thermally-activated intrinsic carriers rather than carriers from either intentionally-doped or unintended impurities or point defects. This is particularly unusual for complex ceramics with volatile cations fabricated across a wide variety of compositions by a number of different groups around the world.<sup>29, 33</sup>

Development of Ni-compatible BaTiO<sub>3</sub>-based multilayer cofired ceramic (MLCC) capacitors with X7R temperature stability (X7R is a designation from the Electronic Industries Alliance, EIA, that indicates a variation of permittivity of no more than  $\pm 15\%$  over the rated operating range of -55 to 125 °C; similarly, Y5V designation applies to capacitance variation less than +22 and -82% between -30 and +85 °C) represents one of the great materials engineering accomplishments of recent decades. This temperature stability is made possible by the development of carefully-controlled compositional gradients that form the well-known core-shell structure within individual grains of the microstructure, resulting in a ‘smearing out’ of the structural phase transitions present in BaTiO<sub>3</sub>. Similarly, though there are significant ongoing efforts to reduce long-term degradation, control of defect chemistry to enable low-pO<sub>2</sub> cofiring with nickel electrodes while retaining reasonably high resistivity is a truly incredible achievement. What makes the properties of BT-Bi(M)O<sub>3</sub> dielectrics especially intriguing is that both this temperature stability and compensation of inevitable charged and mobile defects appear to happen intrinsically, with little to no engineering required on the part of the fabricator.

A number of publications have surveyed the high temperature dielectric performance of various materials systems including several members of the BT-Bi(M)O<sub>3</sub> family, the most recent being from Zeb and Milne.<sup>3</sup> The scope of the present work instead focuses on the structural and microstructural effects of Bi(M)O<sub>3</sub> additions to BT in order to elucidate the origins of the interesting and unusual properties of these materials. Specifically, we highlight recent insights into the local and average atomic structures, detail phase and microstructure development during processing, and discuss proposed mechanisms underlying the observed properties.

## Structure

### Crystallochemical Relations in BaTiO<sub>3</sub> – Bi(M)O<sub>3</sub> Materials

The long-range structure of BaTiO<sub>3</sub> (BT) is well understood, and at 300 K it can be described by the P4mm space group with lattice parameters of  $a = 3.99095(29)$  and  $c = 4.0352(3)$  with a  $c/a$  ratio of 1.011.<sup>37</sup> In tetragonal BT, the Ba<sup>2+</sup> cations are found at the symmetric (0,0,0) unit cell corner positions while the O<sup>2-</sup> octahedral and Ti<sup>4+</sup> cation are shifted in antiparallel directions by  $\sim 0.08$  Å, which is the origin of the spontaneous polarization.<sup>37</sup>

While the structure of tetragonal BT is relatively simple, the structures of Bi-based perovskites are generally more complex, and any ferroelectric properties cannot be attributed exclusively to B-site distortions. Many studies have found that in Bi-based perovskites, the Bi<sup>3+</sup> cation is offset from its symmetric position; this offset of the Bi<sup>3+</sup> cation has been observed in pyrochlores as well, suggesting that this phenomenon is not limited to perovskite structures.<sup>38-40</sup> Several reports on the widely-studied lead (Pb)-free

ferroelectric material  $\text{Na}_{1/2}\text{Bi}_{1/2}\text{TiO}_3$  (NBT) have demonstrated that the  $\text{Bi}^{3+}$  cation is off-centered within its 12-fold  $\text{O}^{2-}$  coordination environment, which creates a bimodal Bi-O bond length distribution.<sup>41-43</sup> In crystallographic refinements, such  $\text{Bi}^{3+}$  displacements (i.e., “static disorder”) are often observed as unusually large atomic displacement parameters in Bi- or NBT-based materials.<sup>44, 45</sup> Furthermore, it has been shown that, in NBT, the direction of the  $\text{Bi}^{3+}$  displacement will reorient to align with an applied electric field.<sup>46</sup> Generally, behavior of the  $\text{Bi}^{3+}$  cation is attributed to its relatively small ionic radius (1.31 Å) compared to other A-site cations like  $\text{Ba}^{2+}$  (1.61 Å) or  $\text{Pb}^{2+}$  (1.49 Å).<sup>47, 48</sup>

When BT is modified with a sufficient amount of  $\text{Bi}(\text{M})\text{O}_3$ , a pseudocubic structure is observed; this transition typically occurs when the mole fraction of  $\text{Bi}(\text{M})\text{O}_3$  is between 0.05 and 0.15.<sup>27, 36, 49-56</sup> In the literature both “cubic” and “pseudocubic” are used to describe the BT- $\text{Bi}(\text{M})\text{O}_3$  phase, and in this section it will be evidenced that pseudocubic is the more appropriate term. We define pseudocubic as the following: a structure which appears cubic by X-ray or neutron diffraction (i.e., no apparent peak splitting), but has one or more of these features: 1) nearly-cubic lattice parameters but atomic displacements within the unit cell that do not obey cubic symmetry; 2) lattice distortions at the local scale which “average out” to cubic (or nearly-cubic); 3) subtle distortions that are not resolvable with the instrument(s) used. Figure 5(a) shows a generalized phase diagram for BT- $\text{Bi}(\text{M})\text{O}_3$  systems. For pure BT at the left side of the phase diagram, the structure from 5-120 °C is tetragonal ( $\text{P4mm}$ ) and at higher temperatures the structure is cubic ( $\text{Pm}\bar{3}\text{m}$ ). All BT- $\text{Bi}(\text{M})\text{O}_3$  material systems discussed here undergo a phase transition at room temperature from the tetragonal  $\text{P4mm}$  phase of  $\text{BaTiO}_3$  to a phase-pure pseudocubic perovskite phase with increasing  $\text{Bi}(\text{M})\text{O}_3$

concentration. This pseudocubic phase is typically maintained to  $\sim 0.4$   $\text{Bi(M)O}_3$  before impurity phases are observed. The  $\text{BT-Bi(Zn}_{1/2}\text{Zr}_{1/2})\text{O}_3$  system is the single example found by the authors where another phase is observed at high  $\text{Bi(M)O}_3$  content; a transition from a pseudocubic phase to an orthorhombic phase in addition to the presence of secondary phases for  $x \geq 0.40$  was reported.<sup>50</sup>

Tolerance factor may be considered as one variable which should influence the concentration at which  $\text{Bi(M)O}_3$  becomes a pseudocubic phase. The tolerance factor,  $t$ , is defined as

$$t = \frac{r_A + r_O}{\sqrt{2}(r_B + r_O)} \quad (4)$$

When equal to 1, the perovskite structure should exhibit the cubic phase.<sup>25,62</sup> When larger than 1, tetragonal phases are expected, and when smaller than 1, rhombohedral or orthorhombic phases are expected.

The tolerance factor of BT is 1.06, which corresponds with the tetragonal phase observed at room temperature. Figure 5(b) shows the compositional limit of the BT-rich  $P4mm$  phase plotted against the tolerance factor of various  $\text{Bi(M)O}_3$  compounds. There is a trend of moderate strength between the two; the  $\text{Bi(M)O}_3$  compounds with lower tolerance factors (i.e., further deviation from the tolerance factor of BT, as shown at the top of Figure 5(b)) exhibit lower compositional limits. This behavior is what one would expect; the lower the tolerance factor for the  $\text{Bi(M)O}_3$  compound, the smaller the fraction of the  $\text{Bi(M)O}_3$  compound required to induce the pseudocubic phase.

It is a curious feature of the  $\text{BT-Bi(M)O}_3$  material systems that they consistently form pseudocubic phases seemingly regardless of the M cation or cations. Not all of the

$\text{Bi(M)O}_3$  compounds discussed here have been synthesized in pure form; in fact, their synthesis routes typically require high pressures, which is why they are often referred to as “unstable perovskites”. Despite this, several have been synthesized in phase-pure form and are reported to exhibit a variety of structures. For example,  $\text{Bi}(\text{Zn}_{1/2}\text{Ti}_{1/2})\text{O}_3$  (BZT), which has been formed under 6 GPa at 900 °C, exhibits a highly tetragonal structure with a  $c/a$  ratio of 1.211 and a spontaneous polarization of  $150 \mu\text{C}/\text{cm}^2$ , of which both values are exceptionally large.<sup>63</sup> In this structure, the  $\text{Bi}^{3+}$  cation is shifted  $0.88 \text{ \AA}$  towards one square face of its 12-fold coordination environment ( $0.4 \text{ \AA}$  further than  $\text{Pb}^{2+}$  is shifted in  $\text{PbTiO}_3$ ), resulting in essentially 4 short Bi-O bonds, 4 intermediate Bi-O bonds, and 4 ‘absent’ Bi-O bonds.<sup>63</sup> The highly tetragonal structure reported conflicts with the rhombohedral or orthorhombic structure expected from the tolerance factor guidelines (for BZT,  $t = 0.925$ ). However, first-principles calculations have demonstrated that the rhombohedral structure is not the lowest energy due to Coulombic repulsion of Bi and Zn, and instead the highly-distorted tetragonal structure is stabilized.<sup>64</sup> Similarly, phase-pure  $\text{Bi}(\text{Mg}_{1/2}\text{Ti}_{1/2})\text{O}_3$  (BMT) has been synthesized at 6 GPa and  $\sim 1000 \text{ }^\circ\text{C}$ .<sup>65</sup> Despite any apparent similarities between BZT and BMT regarding chemistry and processing routes, the structure of BMT is quite different from that of BZT; it is best described by the orthorhombic  $\text{Pnmm}$  space group and exhibits antiphase tilting as well as antiferroelectric-like displacements of the  $\text{Bi}^{3+}$  cation of  $\sim 0.21 \text{ \AA}$ .<sup>65</sup> First-principles calculations also report octahedral tilts and off-centering of both the  $\text{Bi}^{3+}$  and B-site cations for BMT.<sup>66</sup> In this case, the tolerance factor guidelines can accurately predict the structure of BMT ( $t = 0.929$ ); this is attributed to the weaker Coulombic repulsion between Bi and Mg.<sup>64</sup> BZT and BMT are just two examples of “unstable”  $\text{Bi(M)O}_3$  perovskites that can be alloyed

with BT, and though they have very different structures in pure form, they have similar tolerance factors and both induce a pseudocubic structure at  $x \approx 0.07$  in  $(1-x)\text{BaTiO}_3-x\text{Bi(M)O}_3$ .

Within the class of  $\text{BT-Bi(M)O}_3$  materials, a recent study on  $0.6\text{BaTiO}_3-0.4\text{BiScO}_3$ , which used a combination of multiple experimental datasets (X-ray and neutron total scattering and pair distribution functions (PDFs), extended X-ray absorption fine structure (EXAFS) for the Bi and Sc edges, and diffuse scattering in electron diffraction patterns), has revealed many structural details. In this composition, the larger  $\text{Ba}^{2+}$  and  $\text{Sc}^{3+}$  cations create oversized A-site cages for the  $\text{Bi}^{3+}$  ion, which leads to off-centering of the  $\text{Bi}^{3+}$  cations in order to create short Bi-O bonds and relieve the tensile bond strain.<sup>67</sup> It was found that both  $\text{Bi}^{3+}$  and  $\text{Ti}^{4+}$  cations prefer displaced sites with specific distributions (14 sites for  $\text{Bi}^{3+}$  and 8 sites for  $\text{Ti}^{4+}$ ) and that there are correlations among the directions of the displacements.<sup>67</sup> The authors of the study proposed dynamic hopping among the different sites as a possible mechanism for dielectric relaxation. The concurrent hopping of both  $\text{Bi}^{3+}$  and  $\text{Ti}^{4+}$  within this chemically disordered system would have a very broad distribution of relaxation times, which concurs with the strong frequency dispersion found in the relative permittivity as a function of temperature as well as the anomalously-high Vogel-Fulcher activation energies that led to these materials being referred to as weakly-coupled relaxors.<sup>1, 36</sup> The preference of rattling  $\text{Bi}^{3+}$  ions to displace to specific sites in terms of both angle and displacement in much the same way as the  $\text{Ti}^{4+}$  ions inspired the phrase “double rattling ion model” to describe the phenomenon. This is in contrast to the manner in which  $\text{Pb}^{2+}$  ions are commonly described to displace to varying magnitudes in somewhat less-restricted directions in Pb-

based relaxor dielectrics. It should be noted, however, that an earlier computational study did suggest a weak preference for distinct sites for displaced  $\text{Pb}^{2+}$  ions,<sup>68</sup> so it is possible that the apparent differences between the  $\text{Bi}^{3+}$  and  $\text{Pb}^{2+}$  displacements in these systems are more related to experimental resolution and magnitude of effects than to completely distinct phenomena.

### Case Study on a Representative System

In this section we present a detailed structural study on the system  $(1-x)\text{BT}-x\text{BZT}$ , which is a representative  $\text{BT}-\text{Bi}(\text{M})\text{O}_3$  system.<sup>69</sup> Previously, the phases present in the  $(1-x)\text{BT}-x\text{BZT}$  system have been reported to be a tetragonal phase for  $x \leq 0.08$  and a pseudocubic phase for greater BZT content.<sup>27</sup> The results here focus on two compositions of  $(1-x)\text{BT}-x\text{BZT}$ , one on each side of the phase boundary, using high resolution X-ray diffraction (HRXRD) and neutron total scattering, which is converted into PDFs. HRXRD yields the average, long-range structure of these materials, and the exceptionally high resolution of the synchrotron X-ray diffractometer allows the observation of subtle structural distortions.<sup>70</sup> In contrast, analyses of the neutron PDFs reveal the ‘local structure’ of the material (i.e., the local coordination and bonding environments and atom-atom distances from 0 to  $\sim 75$  Å). Both measurements are spatial averages (e.g., could not differentiate homogeneous from core-shell-type of heterogeneous structures) as they record the signal from the entire sample volume.

HRXRD patterns were measured on beamline 11-BM at the Advanced Photon Source at Argonne National Laboratory.<sup>70</sup> Crushed powders of each composition were loaded into Kapton capillaries and spun to achieve improved powder averaging statistics.

XRD patterns were recorded at room temperature with a wavelength of 0.413132 Å, using standard data collection protocol (30 keV, multi-detector range covering approximately 0.5 to 52° in 2 $\theta$ ).

Samples for the PDF measurements originated from the same batch of powders as those used in the HRXRD experiments. Approximately 6-8 g of each powder was loaded into a vanadium can and neutron total scattering data were recorded for approximately 3 h at room temperature on the neutron total scattering powder diffractometer NPDF at the Lujan Neutron Scattering Center at Los Alamos National Laboratory.<sup>71</sup> Using the program PDFgetN (software used to calculate a PDF from neutron total scattering data), the data were corrected for instrument background, incident neutron spectrum, absorption and multiple scattering, were normalized, and the experimental  $G(r)$  (i.e., the experimental PDF) were extracted.<sup>72</sup> Total scattering data are typically presented as a function of the scattering momentum transfer  $Q$ , where  $Q = (4\pi \sin \theta)/\lambda$ , in which  $\theta$  is one half of the scattering angle  $2\theta$  and  $\lambda$  is the radiation wavelength. Based on the inspection of noise levels in the data, the total scattering data were terminated at  $Q = 34 \text{ \AA}^{-1}$ . Due to the high resolution at high  $Q$  of NPDF, PDFs have clearly defined atom-atom distances (pair correlations) to a high  $r$ -range (approximately 100 Å).

Combined Rietveld refinements utilizing both the HRXRD and neutron total scattering patterns were performed using the refinement package GSAS with the EXPGUI interface.<sup>73,74</sup> For a given space group or combination of space groups, the lattice parameters, atomic positions, atomic occupancies, and isotropic displacement parameters were refined. Least-squares refinements of the PDF data were performed



using PDFgui.<sup>75</sup> Additional details regarding the experiment and analyses can be found in Ref. <sup>69</sup>.

The HRXRD and neutron total scattering patterns for 0.94BT-0.06BZT, which lies on the tetragonal side of the phase boundary, revealed additional structural complexity compared to prior studies. As shown in the top panel of Figure 6, three peaks were observed for the (110) and (200) diffraction reflections, indicating that either an additional phase is present or the symmetry is lower than P4mm, as a pure P4mm phase would result in only two peaks for these diffraction reflections. A combined Rietveld refinement using both the HRXRD and the neutron total scattering data revealed that a two-phase mixture of tetragonal and cubic phases best fits the data (70 wt% P4mm, 30 wt% Pm $\bar{3}$ m), as shown in Figure 6. By utilizing a higher resolution probe, it was discovered that this composition actually lies within a two-phase region, and is not purely a tetragonal phase.

For 0.8BT-0.2BZT, the HRXRD and neutron total scattering patterns are shown in Figure 7. A combined Rietveld refinement was first attempted in the cubic Pm $\bar{3}$ m space group, as there is only one peak for each diffraction reflection. However, this model did not satisfactorily model the diffraction pattern. If the structure is pseudocubic and not truly cubic, it is likely that a lower symmetry space group would better model the pattern. Therefore, a combined Rietveld refinement with the P4mm space group was trialed and found to provide a much improved fit. The c/a ratio remained nearly cubic (1.000141(5)), but the atomic positions of the B-site cations and the O<sup>2-</sup> anions were displaced from those of the cubic perovskite structure (Pm $\bar{3}$ m). The B-site cation (Zn/Ti) was shifted from the high-symmetry position (0.5, 0.5, 0.5) by ~0.018 (in fractional

coordinates) in the [001] direction. The O1 and O2 atomic displacements had a similar magnitude but were displaced in the opposite direction. This atomic arrangement is similar to that of BaTiO<sub>3</sub>.

PDFs are sensitive to local-scale correlations of atomic displacements which are not discernable in a long-range structure determined from Bragg diffraction. PDFs are calculated from the sine Fourier transform of the total scattering data and yield the probability of atom-atom pairs as a function of distance,  $r(\text{\AA})$ <sup>76</sup>. The PDFs of 0.94BT-0.06BZT and 0.8BT-0.2BZT were analyzed using a small-box modeling approach in the program PDFgui.<sup>75</sup> It was found that both compositions were best modeled through the use of a single P4mm phase. In the case of 0.94BT-0.06BZT, the inclusion of the secondary cubic phase observed via Bragg diffraction did not improve the PDF fit. The  $c/a$  ratio for the single tetragonal phase is 1.00896(2), which is similar to that of pure BT. For 0.8BT-0.2BZT, it was found that the cubic Pm $\bar{3}$ m model did not adequately model the PDFs, and changing to the P4mm space group provided a much improved fit. Notably different than the long-range refined structure, the  $c/a$  ratio is 1.00663(1), which is much larger than the pseudocubic  $c/a$  ratio obtained from the Rietveld refinement and more similar to that of 0.94BT-0.06BZT and pure BT.

As a result of the fact that the long-range structures determined from Bragg diffraction and the local structures determined from the PDFs are different, it can be said that (1-x)BT-xBZT exhibits a length-scale dependent structure. The local structure differs from the intermediate and long-range, average structures. In order to characterize this length scale dependence, a box-car fitting technique was applied to the neutron PDFs in order to refine the lattice parameters as a function of length scale. In the box-car fitting

method, r-ranges of 10 Å (1-10, 5-15, 10-20, 15-25...70-80 Å) were sequentially refined. The r-ranges selected were larger than a single unit cell (~4 Å) and overlapped with one another. This analysis method allowed the structure from the smallest length scale observable (<10 Å) to the longest length scale (80 Å) to be refined. For example, in the 1-10 Å range, the structure was refined based on atom-atom distances which are 0-2.5 unit cells apart. Any unit cell-level distortion would be apparent. Conversely, for the 70-80 Å range, the structure was refined based on atom-atom distances which are 17.5-20 unit cells apart. If there were nanoscale regions in the material with distortions that varied over a smaller length scale (i.e., polar nano-regions), the distortions would be averaged out when considering atom-atom distances that are ~20 unit cells apart, and the structure would appear pseudocubic.

The box-car fits for four 10 Å ranges (1-10, 10-20, 20-30, and 60-70 Å) are shown for 0.80BT-0.20BZT in Figure 8. The goodness of fit ( $R_w$ ) and  $c/a$  ratios are listed in each panel. The  $c/a$  ratios decrease with increasing r-ranges, from 1.0138(2) for the 1-10 Å range to 1.00049(4) for the 60-70 Å range. The lattice parameters as a function of length scale for both 0.94BT-0.06BZT and 0.8BT-0.2BZT are shown in Figure 9 as the solid symbols, while the lattice parameters determined from the combined Rietveld refinement are shown as solid blue lines for the tetragonal phases and a dashed pink line for the cubic phase in 0.94BT-0.06BZT. The lattice parameters exhibit a slight increase in tetragonality at the shortest length scales for 0.94BT-0.06BZT, but then converge to the long-range lattice parameters. For 0.8BT-0.2BZT, the behavior is very different. At the shortest length scale, the same tetragonal distortion is present, but decreases with

increasing length scale. For atom-atom distances  $> 40 \text{ \AA}$ , the lattice parameters are close to the pseudocubic lattice parameters determined from the combined Rietveld refinement.

This analysis indicates that there are local-scale regions of tetragonal distortions which are disrupted at increasing length scale, either through a variation in domain orientation (the 2<sup>nd</sup> definition of pseudocubic) or because of separation by a cubic region. Either case is similar to the polar nano-regions (PNRs) thought to be present in canonical relaxors such as PMN. At the long-range scale, a pseudocubic lattice is observed, while the nanometer-scale reveals the tetragonal distortions and atomic displacements. It appears that  $\text{Bi}^{3+}$  and  $\text{Zn}^{2+}$  contribute to local lattice distortions (up to 10 unit cells), but also induce sufficient disorder to disrupt the long-range ferroelectric symmetry present in unmodified  $\text{BaTiO}_3$ .

To conclude the discussion of the structure of these materials, the  $\text{BT-Bi(M)O}_3$  systems discussed herein exhibit similar behavior in terms of both phase transitions and dielectric properties. It appears that the addition of any one of many  $\text{Bi(M)O}_3$  compounds (or combination of compounds) to BT introduces sufficient chemical and positional disorder to disrupt the long-range ferroelectric order present in pure BT, which is observed as a transition to a pseudocubic phase. The composition or compositional range where this transition occurs depends at least partly on the sizes of the B-site cations of the  $\text{Bi(M)O}_3$  compound, as represented by phase boundary versus tolerance factor trend shown in Figure 5. This transition to a pseudocubic phase is observed in the case of 0.8BT-0.2BZT, where the long-range structure is determined by Rietveld refinement of HRXRD and neutron diffraction patterns. However, a local-structure probe reveals that the presence of short-range distortions is maintained – likely in part by the tendency of

$\text{Bi}^{3+}$  to be offset from the A-site high-symmetry position and towards one side of the 12-fold  $\text{O}^{2-}$  coordination environment.

## Processing

Understanding the crystallography and structural origins of the attractive dielectric response of BT-Bi(M)O<sub>3</sub> materials is crucial from a scientific perspective, but from an application standpoint, it means little unless functional parts can be manufactured. The potential for these materials as complements to the traditional X7R and COG classes of capacitor dielectrics was recognized early, so significant efforts have gone into exploring compositional and processing modifications to improve dielectric properties,<sup>2, 19, 56, 57</sup> as well as into fabricating proof-of-concept prototype capacitors.<sup>15, 18, 77, 78</sup>

Based upon reported processing conditions and resulting densities, optimum sintering temperatures decrease with increased Bi(M)O<sub>3</sub> content, with most reports focusing on sintering ceramic pellets of  $(1-x)\text{BaTiO}_3-x\text{Bi(M)O}_3$  with  $0.1 \leq x \leq 0.3$  at temperatures between 1100 and 1200 °C. Significant fractions of Bi-containing species enhance densification and reduce the required sintering temperatures relative to pure BaTiO<sub>3</sub>, but bring additional processing complications. For one, inspection of an Ellingham diagram (Figure 10) immediately indicates an enormous thermodynamic challenge for cofiring Bi-containing dielectrics with base metal electrodes: equilibrium reduction of Bi<sub>2</sub>O<sub>3</sub> to metallic Bi occurs at oxygen partial pressures essentially identical to those for Cu<sub>2</sub>O/Cu and roughly 5 orders of magnitude higher pO<sub>2</sub> levels than NiO/Ni.

Thus, it seems that any scheme for successfully cofiring BT-Bi(M)O<sub>3</sub> with base metal electrodes will need to rely more on kinetic hindrance than thermodynamic stability.

Even cofiring with precious metal electrodes is not necessarily trivial. Wang and Huebner reported on extensive reactions of Ag/Pd electrodes with various Bi-based dielectrics,<sup>79,80</sup> and Ogihara et al. noted a marked decrease in performance for 0.7BaTiO<sub>3</sub>-0.3BiScO<sub>3</sub> (0.7BT-0.3BS) MLCCs cofired with Pt electrodes at 1250 °C.<sup>36</sup> However, Raengthon et al. saw very little difference in performance between 0.5BT-0.25BZT-0.25BS pellets and MLCCs of the same composition cofired with 0.7Ag-0.3Pd electrodes at 1000 °C.<sup>15</sup> To explore this phenomenon further, we report here the case study on the cofiring of physically large high voltage MLCCs consisting of 0.8BT-0.2BZT dielectric layers with Pt electrodes. Despite an optimized binder burnout process in flowing O<sub>2</sub> that was monitored by in situ residual gas analysis (Figure 11, RGA 300, Stanford Research Systems, Sunnyvale, CA), parts sintered at 1200 °C for 6 h showed catastrophic bubbling and delamination (Figure 12). Using the same RGA setup during sintering revealed the evolution of O<sub>2</sub> beginning ~1020 °C (Figure 13), which corresponded closely to the temperature at which an optical camera focused on the sample in the center of the tube furnace observed blister formation. Reducing the sintering temperature to 1000 °C avoided such interactions with the Pt electrodes and produced relatively dense (~95 %) dielectrics with properties largely comparable to ceramic disks sintered to full density at 1120 °C (Figure 14).

The value of in situ process monitoring is certainly not limited to sintering. Even calcination of BT-Bi(M)O<sub>3</sub> materials has been found to be non-trivial. For example, Triamnak et al. described both in situ and quenched ex situ studies of the complex phase

formation during calcination of 0.8BT-0.2BZT and 0.85BT-0.15BZT powders.<sup>81</sup> Related subsequent studies (Figure 15) have verified the findings of the earlier work and even suggest the possibility of two closely-related but distinct perovskite phases (or, potentially, polymorphs of the same phase) following calcination. Figure 15(a) summarizes an in-situ high-temperature XRD study (performed at CoorsTek Advanced Ceramics, Bruker D8 Discover, Anton Parr HTK-2000N hot stage), during which precursor powders reacted to form a (presumably) solid solution of 0.8BT-0.2BZT (denoted as “BaTiO<sub>3</sub> (SS)” on the figure). The reduction in required processing temperatures compared to pure BaCO<sub>3</sub> + TiO<sub>2</sub> → BaTiO<sub>3</sub> is a direct consequence of the intermediate phases accelerating decomposition of BaCO<sub>3</sub>. In addition, note that there are active redox reactions taking place throughout this process, as some of the Bi<sup>3+</sup> introduced as Bi<sub>2</sub>O<sub>3</sub> is oxidized to Bi<sup>5+</sup> in BaBiO<sub>3</sub> (a perovskite in which Bi occupies the B-site with equal amounts of Bi<sup>3+</sup> and Bi<sup>5+</sup>) and later reduced to occupy the A-sites of Bi<sub>4</sub>Ti<sub>3</sub>O<sub>12</sub> and BaTiO<sub>3</sub> (SS) as Bi<sup>3+</sup>. Further, the peak-splitting that is observed in the BaTiO<sub>3</sub> (SS) phase upon consumption of the last of the Bi<sub>4</sub>Ti<sub>3</sub>O<sub>12</sub> phase (shown in more detail for the (110) reflection in Figure 15(b,c), but present for all peaks) suggests the existence of multiple phases or at least multiple polymorphs, even at processing temperatures.

Figure 16 schematically illustrates the reaction pathways observed for the formation of the apparent solid solution of 0.8BT-0.2BZT. It should be noted that while ZnO likely plays an important role in the phase evolution of these materials, because of its low atomic number and relatively small mole fraction, diffraction studies have

provided essentially no information about its incorporation during calcination, so it does not appear in Figure 16.

Such subtle heterogeneity may explain—at least in part—the common occurrence of multicolored calcined powders of these systems; Figure 17 shows one example of such an occurrence. Using XRD and x-ray fluorescence (XRF), no definitive difference in composition or structure can be claimed between the different colored powders, at least within the measurement threshold for each technique (Figure 17). Such optical heterogeneity has not been previously reported in the literature, but offline conversations with other research groups have indicated that similar multicolor powders have been observed for, at the very least, various ratios of BT-BZT, BT-BMT, BT-BS, and BT-BZT-Bi(M)O<sub>3</sub> where M=Sc, Al, Fe, Y. Based upon the assumption that Bi (and Zn, when present) ions are the most mobile species at calcination and sintering temperatures, the consensus working hypothesis is that very small relative amounts of Bi segregation leads to the observed color changes.

Both optical and electrical properties can be extremely sensitive to defect chemistry, so it seems a reasonable assumption that the variability observed in calcined powders would correspond to comparable variability in the electrical response of sintered parts. Extensive optical and chemical studies could presumably clarify the mechanisms involved, but the fact that densification and electrical behaviors of these multicolored powder batches are indistinguishable from those of optically homogeneous batches seems to have limited motivation for deeper study of powders.

The majority of published reports of BT-Bi(M)O<sub>3</sub> ceramics have focused on the properties without many details about processing and microstructure, but the



microstructures that have been published are mostly consistent with Figure 18. Dense microstructures with 2-5  $\mu\text{m}$  grain sizes are typical for compositions with  $\geq 20\%$   $\text{Bi(M)O}_3$  additions (those with lower amounts of  $\text{Bi(M)O}_3$  commonly have finer grains unless the sintering temperature was  $>1300\text{ }^\circ\text{C}$ ). The most striking features of these microstructures, however, are not the density or grain sizes but rather the contrasting regions within the grains. When imaged with secondary electrons, the surfaces appear essentially featureless if well-polished or similar to Figure 18(a) if thermally etched to accentuate the grain boundaries. When well-polished samples are imaged with backscattered electrons, however, compositional heterogeneity becomes apparent (Figure 18(b)). For example, Figure 18(b) was collected using the in-lens backscatter detector on a Zeiss Supra 55VP; thus, contrast from one grain to another is dominated by differences in grain orientation due to electron channeling effects, whereas contrast within an individual grain is caused by differences in average atomic number, with regions of higher atomic number appearing brighter.

Others have seen similar effects, but what is much more frequently reported is the development and then disappearance of a more traditional core-shell structure akin to that which has been engineered into traditional X7R-type dielectrics. While the origins may be similar from the chemical mechanism(s) perspective, the type of heterogeneity seen in X7R-type dielectrics (see, for example, Figure 3(c) and (d) from <sup>36</sup>) is distinct from that in Figure 18(b) because the cores of the grains clearly show ferroic domain walls while the differences between the ‘core’ and ‘shell’ of the grains in Figure 18(b) appear to be purely compositional with no evidence of any domains.

TEM analysis (FEI Tecnai G2 30 with STEM-EDS and Axsia multivariate statistical analysis software) revealed just how subtle the compositional variation is. As shown in Figure 19, regions that exhibit a high degree of contrast in the SEM, when lifted out via FIB and imaged in the TEM, are somewhat difficult to identify. Quantitative EDS, including non-trivial deconvolution of the overlapping Ba and Ti signals, revealed variations in the Ba/Bi ratio that correlate closely with the image contrast and vary only 2-3% in terms of overall A-site occupancy. Thus, while not at all quantitative, the SEM imaging technique in this case provides a quick and sensitive indication of compositional heterogeneity. Subsequent studies on other samples in the BT-BZT family confirmed the anticorrelated variation of Ba and Bi across the grain core (Figure 20). Most of the grains observed over a wide range of compositions and processing parameter sets showed some amount of increased Bi content in or near grain centers, and often at grain boundaries, though a number showed the inverse, with Bi-rich rings between Ba-rich grain centers and boundaries.

Deviations from stoichiometry affect not only electrical behavior (as discussed in detail in the next section), but by controlling the rate limiting step for diffusion, can also significantly alter processing behavior. With this in mind, an extensive study of the effects of acceptor and donor doping on BT-BZT ceramics was undertaken, again as a representative system for the broader BT-Bi(M)O<sub>3</sub> family. Regardless of the dopant(s) used—or, within the limits of the study, their amounts—the resulting microstructures could be grouped into two types as exemplified by Figure 21(a) and (b).

Donor doped specimens (Figure 21(a)) exhibited somewhat smaller average grain sizes (typically 1-2  $\mu\text{m}$  after sintering at  $\sim 1150$  °C for 6 h) than nominally stoichiometric

samples and, while they exhibited a great deal of (qualitative) heterogeneity with occasional sharp interfaces, the dominant characteristic of the intra-grain contrast is a rather graded transition from one level of brightness to another. Some grains contain dark cores, others light cores, and some show complex mixtures of the two extremes, but in nearly all cases, the interfaces appear to be graded and indistinct. On the other hand, acceptor-doped samples typically exhibited somewhat larger grains on the order of 5-10  $\mu\text{m}$ . As seen in Figure 21(b), the compositional contrast within each grain is significantly less than that seen in the donor doped samples, but the contrasting regions that are present are very distinct with sharp boundaries between light, dark, and intermediate (nominal grain background). Dark contrast (low atomic number) regions are frequently found within light (high atomic number) regions, with morphologies reminiscent of precipitates. Finally, while BT-Bi(M)O<sub>3</sub> samples of all types frequently have thin high-atomic-number grain boundaries, these boundary layers are noticeably thicker for the acceptor-doped samples and are often accompanied by bright pockets at triple points. It is not clear whether the increase in thickness represents nominally the same volume of high atomic number grain boundary material concentrated around a smaller number of large grains or whether there is actually more of this grain boundary phase present in the acceptor-doped samples.

Clearly the presence of significant amounts of Bi substantially affects the phase evolution and microstructure development in BT-Bi(M)O<sub>3</sub> ceramics. In particular, the diffusion and occupancy of Bi seems to be a particularly valuable topic for further study.

## **Properties**

As mentioned in the introduction, BaTiO<sub>3</sub>-based relaxors are obvious candidates for dielectric applications, especially for demanding applications that require high voltages, high temperatures, and temperature-stable permittivity values.<sup>3</sup> Relaxors based on solid solutions of BaTiO<sub>3</sub> with Bi(M)O<sub>3</sub> exhibit excellent electrical properties, with some unusual characteristics compared to conventional high permittivity dielectrics including high energy density values, improved insulation resistance, and temperature and electric-field stable dielectric properties, as discussed in this section.

Figure 22 shows some examples of relaxor BT-Bi(M)O<sub>3</sub> ceramics, where M = (Zn,Ti), (Zn,Ti,Sc), (Sc,Ti), Sc and (Ni,Ti).<sup>18, 26, 82</sup> The relative permittivity values of all of these solid solutions remain large ( $\epsilon_r \sim 1000$ ) and relatively stable as compared to undoped BT, which has a characteristic sharp phase transition at the Curie point ( $T_C$ ).<sup>83</sup> This crossover from normal ferroelectric behavior for BT to relaxor behavior in these solid solutions is intimately related to the destabilization of long-range dipole order (i.e., domains) and the formation of PNRs. It has been argued that the PNRs form due to random fields generated as a result of structural and charge inhomogeneities driven by homogeneous or heterogeneous cation substitutions on the A-site or B-site in the parent normal ferroelectric (here, BaTiO<sub>3</sub>), and that the random interaction between the PNRs is key to the destabilization of domains. Interestingly, these PNRs are nucleated at a temperature (Burns temperature,  $T_B$ ) much higher than the temperature of maximum permittivity ( $T_{max}$ ). While  $T_C$  for BaTiO<sub>3</sub> is known to be  $\sim 125$  °C, the Burns temperature for relaxor BZT-modified BT, for example, has been reported to be as high as  $\sim 400$  °C.<sup>84</sup> As discussed earlier, the local symmetry of these PNRs can be polar and quite different from the apparent macroscopic symmetry. At the same time, in the absence of any

external stimuli, these PNRs are randomly oriented and the net polarization remains close to zero. As the temperature is decreased, these PNRs remain dynamic with their dipole moments easily fluctuating thermally between equivalent polarization states, as was proposed by the polar-glassy model inspired from the superparaelectric model and superparamagnetism.<sup>20, 23</sup> These relaxors have been labeled ergodic relaxors (ER) in the literature, and they typically have sufficient energy to return back to their original state after an external excitation is applied and then subsequently removed.<sup>85</sup> As the temperature is reduced further, the PNRs within these relaxors grow in size and number, and the interactions between them grow stronger. They typically pass through a maximum in permittivity ( $T_{\max}$ ), which is usually broad and a direct result of the wide distribution of relaxation times due to a wide distribution of the sizes of PNRs and random interactions between them.<sup>86</sup> The average size of these PNRs abruptly increases and the number decreases at the freezing temperature ( $T_f$ ) which represents the temperature at which the dynamics of some PNRs become slow enough to freeze and transition to a glassy-like non-ergodic state (NR).<sup>86, 87</sup> Unlike ER relaxors, NR relaxors usually transform irreversibly to a ferroelectric (FE) state on application of an external stimulus, such as an electric field.

While this is a rather simplistic review of the evolution of PNRs with temperature, it helps to highlight the differences between canonical relaxors (e.g., Figure 22(d)) and a normal ferroelectric material such as BT. Several advanced models have also been developed over time such as the random-site model, the spherical random-bond-random-field model and others, and can be used to gain further insights into the relaxor phenomenon.<sup>88, 89</sup> There might also be more complexities present in certain relaxor

materials than the simple model presented above. One peculiar example is that of BT-BiScO<sub>3</sub>, which has been shown to exhibit “weakly-coupled behavior” as discussed earlier, and a re-entrant behavior (Figure 23) analogous to re-entrant magnetic spin glass systems.<sup>90, 91</sup> It can be seen that the remanent polarization first increases upon lowering the temperature and reaches a maximum, which was interpreted to be a result of a long-range dipole ordered state. A disordered phase then develops from this ferroelectric-like state, which is unusual because most relaxors develop from a high-temperature paraelectric phase.<sup>91</sup> Alternate complex scenarios can exist in other relaxors, the details of which can be found in some excellent review papers.<sup>82, 86, 92, 93</sup>

As seen in Figure 1 and discussed broadly in the introduction, addition of BZT to BT results in a gradual transition to a relaxor state (Figure 1(c)), via a DPT (Figure 1(b)). As discussed, the behavior of DPT can be described by Equation (1), and the relaxors in general follow Vogel-Fulcher law (Equation 3). Raengthon et al. recently showed that tolerance factor can be used as a guide to tailor TCε in BT- Bi(M)O<sub>3</sub> ceramics.<sup>25</sup> Recall from Figure 5 that the solubility of Bi(M)O<sub>3</sub> species in BaTiO<sub>3</sub> is also lower for Bi(M)O<sub>3</sub> species with small tolerance factors.

Typically, ferroelectric perovskites exhibit high relative permittivity values (>1000), and since the mechanisms controlling the permittivity and macroscopic polarization are related, typically these also exhibit high values of macroscopic polarization on application of an external electric field. Some relaxor materials can exhibit an electric field-induced phase transition to a ferroelectric state on the application of an electric field, which results in increased polarization and strain values.<sup>85</sup> The ER relaxors (especially those with T<sub>f</sub> below room temperature) are of particular interest, as

they can exhibit a reversible phase change with electric field and negligible remanent polarization. At moderate fields, an approximately linear dielectric response is observed for these relaxors, where the polarization,  $P$ , can be given by,  $P = \epsilon_0 \chi_1 E$ , where,  $\epsilon_0$  is the permittivity of free space and  $\chi_1$  is the linear susceptibility of the material. This is technologically important for high energy-density applications, since the energy density per unit volume ( $U_{vol} = \int E dP$ ), which can be calculated by the area enclosed by the P-E loop (decreasing field) and the polarization axis, is enhanced (Figure 24) versus a hysteretic normal ferroelectric because of the tiny remanence associated with relaxors. In recent years, multilayer ceramic capacitors (MLCCs) have been fabricated based on these (ergodic) relaxor BT-Bi(M)O<sub>3</sub> ceramics that exhibit excellent energy density values and which remain relatively insensitive to temperature.<sup>18, 94</sup> At room temperature and an applied electric field of 350 kV/cm, the 0.7BT-0.3BS and 0.85BT-0.15BZT MLCCs had energy density values of  $\sim 3 \text{ J/cm}^3$ , which was noticeably higher than some other commercially available MLCC devices (Figure 24 (b)).

Several members of the BT-Bi(M)O<sub>3</sub> family of ceramics exhibit excellent dielectric properties that are intrinsically stable at high temperatures and/or under strong electric fields. Operating under large applied fields obviously requires a high breakdown strength; because many target applications operate under a baseline dc field with a superimposed ac ripple, both a high dc resistivity and a low tangent delta at operating frequencies are important to avoid self-heating and thermal runaway. Additionally, the migration of ionic species under field may only contribute a small amount to initial dc conductivity, but can lead to catastrophic degradation of properties over time. Because of the activated nature of charge transport, all of these mechanisms are made easier (and

therefore of greater concern) at elevated temperatures. Likewise, all of this charge transport is intimately related to the underlying defect chemistry of these BT- Bi(M)O<sub>3</sub> ceramics. Put simply, using dielectrics at high fields and elevated temperatures requires minimization of the concentration of electrically active defects.

A systematic study of transport properties by Kumar et al. on polycrystalline BT-BZT and a similar study on SrTiO<sub>3</sub>-BZT (ST-BZT) demonstrated that the addition of a small mole fraction of BZT improved the bulk resistivity value by multiple orders of magnitude (Figure 25 (a,b)).<sup>95</sup> The activation energy values, obtained from the slopes of the Arrhenius plots, also increased from ~1 eV for BT to values very nearly equal to half of the optical band gap (~3.1 eV), as determined from diffuse reflectance measurements.<sup>95</sup> These results were consistent with other studies based on different BT-Bi(M)O<sub>3</sub> materials, pointing to the accommodating nature of this family of dielectrics<sup>15, 56, 96, 97</sup>. Such high resistivity values together with large activation energies for conduction suggest that charge transport in these BT-Bi(M)O<sub>3</sub> dielectrics is dominated by thermal activation of intrinsic electron-hole pairs or similar carrier generation mechanisms as opposed to the defect-dominated conduction that is common in BaTiO<sub>3</sub>.<sup>98</sup>

Resistivity measurements in different atmospheres can be used to determine the dominant conduction species in a material. Cation conductivity in BaTiO<sub>3</sub> and related materials is negligible compared to that of electrons, holes, and oxygen vacancies, so we can focus our attention on these three mobile species. Because the mobilities of electrons and holes are much higher than for oxygen vacancies<sup>99</sup> and because laboratory experiments can normally be performed close to the conductivity minima for BT-based ceramics<sup>100</sup>, conduction controlled by oxygen vacancies is independent of pO<sub>2</sub>, whereas



conduction dominated by electronic species will show a direct relationship with  $pO_2$  for n-type conduction or an inverse relationship with  $pO_2$  for p-type conduction (Figure 26(b)).

The known p-type behavior of  $BaTiO_3$  was demonstrated through  $pO_2$ -dependent ac impedance spectroscopy (Figure 26(a)). Bulk resistivity values, determined from the x-axis intercept of the high frequency arc in Nyquist plots, decreased with increased oxygen partial pressure<sup>101</sup>. For  $BaTiO_3$  and similar titanate perovskites, the p-type behavior is considered to be a consequence of unintentional low valence impurities which are present in titania, barium carbonate, or other cation precursors and high temperature processing conditions that result in frozen-in cation vacancies.<sup>102-104</sup> These acceptors can be compensated by holes or oxygen vacancies which can lead to a p-type behavior at high oxygen partial pressure ( $pO_2$ ) according to following defect reaction:



where,  $V_O^{\bullet\bullet}$  represents doubly-ionized oxygen vacancies,  $O_O^X$  represents an oxygen ion located on an oxygen lattice site, and  $h^{\bullet}$  represents a hole.

In considering the observed improvement in resistivity on adding BZT to  $BaTiO_3$  or  $SrTiO_3$ , the results of Kumar et al. suggest that the mechanism is either due to a reduction in the source of holes or unintentional donor doping leading to compensation of holes.<sup>101</sup> In other words, either the concentration of cation vacancies was reduced, which was a possibility since the sintering temperatures of the BZT-containing ceramics were lower than typical for pure  $BaTiO_3$ , or there should be an alternative charge compensation mechanism present to compensate for acceptor impurities or cation

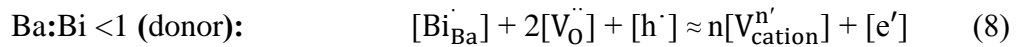
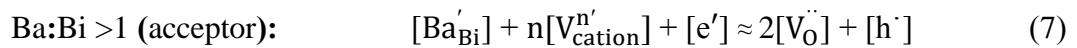
vacancies. Some of the possible candidates that could act as effective donors include oxygen vacancies, pentavalent bismuth on the B-site, and loss of volatile zinc during processing resulting in an effective excess of A-site  $\text{Bi}^{3+}$ .<sup>101</sup>

Impedance spectroscopy on BT-BZT ceramics as a function of  $p\text{O}_2$  showed that the resistivity increased with  $p\text{O}_2$ , revealing that the conduction was still electronic, but dominated by electrons (Figure 27(a)),<sup>101</sup>, suggesting the following dominant compensation reaction:



where,  $e'$  represents an electron. The observation of a p-type to n-type transition with the addition of small amounts of BZT to  $\text{BaTiO}_3$  was further supported by Seebeck measurements (Figure 28)<sup>97, 101</sup> and corroborated the hypothesis that BZT additions appear to be effectively donor doping the  $\text{BaTiO}_3$  and reducing the concentration of holes. Similar results were obtained for ST-BZT ceramics. Adding  $\text{BiScO}_3$  instead of  $\text{Bi}(\text{Zn}_{1/2}\text{Ti}_{1/2})\text{O}_3$  to  $\text{BaTiO}_3$  similarly reduced the concentration of holes, but fell short of a full transition to n-type behavior (Figure 27(c)), suggesting both that multiple compensation mechanisms are likely acting simultaneously in BT- $\text{Bi}(\text{M})\text{O}_3$  and that unintentional doping and/or volatility associated with Zn may be the key to the p- to n-type crossover. Similar behavior was seen for donor doped  $\text{BaTiO}_3$  by Smyth et al.<sup>105</sup> (Figure 29), in which they showed that on introducing small amounts of donor doping or reducing the amount of acceptor dopants, the conductivity minima shifted towards higher  $p\text{O}_2$ . At larger concentrations of donor doping, however, the conductivity became independent of  $p\text{O}_2$  for a certain temperature range, as expected.<sup>99, 105</sup>

In addition, it has been shown that manipulating the cation stoichiometries in BT-Bi(M)O<sub>3</sub> ceramics by a small amount can have a significant influence on the transport properties.<sup>97, 106</sup> Figure 30 shows Arrhenius plots for three representative non-stoichiometric solid solutions: ST-BZT, BT-BZT and BT-BS. Non-stoichiometry was introduced onto the A-site by adjusting the ratio of Ba<sup>2+</sup> or Sr<sup>2+</sup> to Bi<sup>3+</sup>. Some general observations can be made on inspection of the data shown in Figure 30: (1) effective acceptor doping via a greater-than-stoichiometric (Ba<sup>2+</sup>, Sr<sup>2+</sup>) to Bi<sup>3+</sup> ratio decreased the resistivity by orders of magnitude, (2) effective donor doping via a less-than-stoichiometric Ba<sup>2+</sup> to Bi<sup>3+</sup> ratio improved the resistivity values by orders of magnitude, whereas the ST-BZT analogues remained essentially unchanged. Furthermore, effectively acceptor-doped samples exhibited p-type conduction, while effectively donor-doped samples exhibited n-type conduction.<sup>106</sup> Since acceptor doping (Equation 7) can only be compensated by oxygen vacancies or holes, both of which can lead to increase in conduction, a decrease in resistivity was always observed. The increase in (or, in the case of ST-BZT, maintenance of high) resistivity via donor doping suggests that donors may be compensated in these systems by relatively immobile cation vacancies (Equation 8).



Thus, the most reasonable conclusion to draw from the large amount of defect chemistry-focused work on the BT-Bi(M)O<sub>3</sub> family (and ST-based analogues) is that as long as the total charge of effective donor dopants is equal to or exceeds the total charge of effective acceptor dopants, the resulting net positive charge is compensated by low-mobility cation vacancies, resulting in high resistivity values and large intrinsic-like

activation energies for conduction. This conclusion is consistent with the electrical data as well as optical spectroscopy and limited EPR results, but it seems rather fortuitous that the defect states would form deep mid-band traps across the entire family of these materials, even when 5, 6, or even 7 cations are involved.

The above scenario assumes that the material is homogeneous and is dominated by bulk grain behavior, but recalling Figure 21(a) opens up another intriguing possibility. If the Bi-rich regions are n-type and the Ba-rich regions are p-type (as would be likely if B-site cation diffusion is slower than A-site cation diffusion), and there are no percolating pathways of either type, the net result of electrical transport measurements on bulk ceramics would be intrinsic-like activation energies. Such a scenario would also likely offer such intrinsic-like activation energies and high resistivity values over a much broader range of compositions (in terms of both cation identities as well as ratios) than the deep trap / cation vacancy model. Especially if these BT-Bi(M)O<sub>3</sub> materials are to fulfill their promise as reliable high-operating-temperature dielectrics, it will be important to elucidate the defect mechanisms involved and their long-term evolution under challenging operating conditions.

## **Summary**

Weakly-coupled relaxor dielectrics in the BT-Bi(M)O<sub>3</sub> family show great promise for use at elevated temperatures and/or large operating fields, but a number of scientific and technological issues demand further study. The double rattling ion model<sup>67</sup> can be used to describe the temperature- and frequency-dependence of the polarizability of these materials fairly well, but the underlying mechanisms need to be verified across a broader

compositional range. Similarly, with further study, this concept could enable researchers to devise even better temperature stable and high-permittivity dielectrics across other systems.

Significant additions of  $\text{Bi}_2\text{O}_3$  reduce the processing temperatures required for  $\text{BaTiO}_3$ - and  $\text{SrTiO}_3$ -based dielectrics, but also impose severe restrictions on electrode compatibility for cofiring because  $\text{Bi}_2\text{O}_3$  is thermodynamically incompatible with both metallic Ni and Cu, and Bi-based species are known to react aggressively with both Pt and Pd at common sintering temperatures. Nevertheless, multiple groups have successfully demonstrated the cofiring of BT- $\text{Bi}(\text{M})\text{O}_3$  dielectrics with Ag-Pd electrodes, and efforts to extend the temperature, atmosphere, and electrode compatibility of these dielectrics are ongoing.

The greatest challenges and opportunities associated with the BT- $\text{Bi}(\text{M})\text{O}_3$  family of materials, however, are related to defect chemistry because of its crucial role in processing, charge transport, and long-term reliability under target operating conditions. The surprisingly-robust resistivity and activation energies for charge transport hint at some sort of self-adjusting mechanism for stoichiometry control and defect compensation; while a variety of possible mechanisms have been put forward in this work and elsewhere, more work is required to better understand the mechanism(s) at work as well as the associated impacts on processing and operation.

The incredible ability of the perovskite crystal structure to accommodate a variety of doping and defect schemes, symmetries, and polarization mechanisms has made it one of the favorite crystal chemistry playgrounds of the electroceramist for decades. The rich behavior reported for materials in the BT- $\text{Bi}(\text{M})\text{O}_3$  family and related systems reminds us

yet again that while the simple unit cell and the space-filling grain structure are valuable starting points, even in combination they are insufficient to capture the complexity inherent in many functional materials. These materials highlight the importance of being able to describe, understand, and ultimately control structure and chemistry across length scales from Angstroms to microns.

### **Acknowledgements**

Bonnie B. McKenzie and Dr. Joseph R. Michael of Sandia National Laboratories provided invaluable assistance on the SEM analysis and interpretation; Mia A. Blea-Kirby of Sandia National Labs and Kelsey E. Meyer (formerly of Sandia, now at the University of Virginia) also provided significant technical assistance to this work. Sandia National Laboratories is a multi-program laboratory managed and operated by Sandia Corporation, a wholly owned subsidiary of Lockheed Martin Corporation, for the U.S. Department of Energy's National Nuclear Security Administration under contract DE-AC04-94AL85000.

Portions of the effort for Geoff L. Brennecka, Harlan James Brown-Shaklee, David P. Cann, and Natthaphon Raengthon were supported by the Department of Energy's Office of Electricity Delivery and Energy Reliability through the Energy Storage Program managed by Dr. Imre Gyuk. Geoff L. Brennecka and Michaela A. Beuerlein were supported in part by the State of Colorado Office of Economic Development and International Trade. A portion of the hot-stage microscopy was carried out by Dr. David Hook of CoorsTek Advanced Ceramics. David P. Cann and Natthaphon Raengthon were partially supported by the National Science Foundation under Grant No.

DMR-1308032. Tedi-Marie Usher acknowledges support from the U.S. Department of Commerce under award number 70NANB13H197, and Jacob L Jones from the National Science Foundation under DMR-1445926.

Use of the Advanced Photon Source at Argonne National Laboratory was supported by the U. S. Department of Energy, Office of Science, Office of Basic Energy Sciences, under Contract No. DE-AC02-06CH11357. This work has benefited from the use of NPDF at the Lujan Center at Los Alamos Neutron Science Center, funded by DOE Office of Basic Energy Sciences. Los Alamos National Laboratory is operated by Los Alamos National Security LLC under DOE Contract DE-AC52-06NA25396. The upgrade of NPDF has been funded by the NSF through grant DMR 00-76488.

## References

1. D. P. Cann, C. A. Randall, and T. R. ShROUT, "Investigation of the Dielectric Properties of Bismuth Pyrochlores," *Solid State Commun.*, **100** [7] 529-34 (1996).
2. N. Raengthon and D. P. Cann, "High-K  $(\text{Ba}_{0.8}\text{Bi}_{0.2})(\text{Zn}_{0.1}\text{Ti}_{0.9})\text{O}_3$  Ceramics for High-Temperature Capacitor Applications," *IEEE Trans. Sonics Ultrason.*, **58** [9] 1954-58 (2011).
3. A. Zeb and S. J. Milne, "High Temperature Dielectric Ceramics: A Review of Temperature-Stable High-Permittivity Perovskites," *J. Mater. Sci.: Mater. Electron.*, **26** [12] 9243-55 (2015).
4. K. Hiroshi, M. Youichi, and C. Hirokazu, "Base-Metal Electrode-Multilayer Ceramic Capacitors: Past, Present and Future Perspectives," *Jpn. J. Appl. Phys.*, **42** [1R] 1-15 (2003).
5. D. P. Shay, N. J. Podraza, N. J. Donnelly, and C. A. Randall, "High Energy Density, High Temperature Capacitors Utilizing Mn-Doped  $0.8\text{CaTiO}_3\text{-}0.2\text{CaHfO}_3$  Ceramics," *J. Am. Ceram. Soc.*, **95** [4] 1348-55 (2012).
6. H. Lee, J. R. Kim, M. J. Lanagan, S. Trolier-McKinstry, and C. A. Randall, "High-Energy Density Dielectrics and Capacitors for Elevated Temperatures:  $\text{Ca}(\text{Zr,Ti})\text{O}_3$ ," *J. Am. Ceram. Soc.*, **96** [4] 1209-13 (2013).
7. J. C. Nino, M. T. Lanagan, and C. A. Randall, "Dielectric Relaxation in  $\text{Bi}_2\text{O}_3\text{-ZnO-Nb}_2\text{O}_5$  Cubic Pyrochlore," *J. Appl. Phys.*, **89** [8] 4512-16 (2001).
8. N. J. Smith, B. Rangarajan, M. T. Lanagan, and C. G. Pantano, "Alkali-Free Glass as a High Energy Density Dielectric Material," *Mater. Lett.*, **63** [15] 1245-48 (2009).



9. L. Egerton and D. M. Dillon, "Piezoelectric and Dielectric Properties of Ceramics in the System Potassium—Sodium Niobate," *J. Am. Ceram. Soc.*, **42** [9] 438-42 (1959).
10. J. F. Li, K. Wang, B. P. Zhang, and L. M. Zhang, "Ferroelectric and Piezoelectric Properties of Fine - Grained  $\text{Na}_{0.5}\text{K}_{0.5}\text{NbO}_3$  Lead - Free Piezoelectric Ceramics Prepared by Spark Plasma Sintering," *J. Am. Ceram. Soc.*, **89** [2] 706-09 (2006).
11. K. Singh, V. Lingwal, S. Bhatt, N. Panwar, and B. Semwal, "Dielectric Properties of Potassium Sodium Niobate Mixed System," *Mater. Res. Bull.*, **36** [13] 2365-74 (2001).
12. R. Dittmer, W. Jo, D. Damjanovic, and J. Roedel, "Lead-Free High-Temperature Dielectrics with Wide Operational Range" *J. Appl. Phys.*, **109** 034107 (2011).
13. M. Kosec, B. Malič, A. Benčan, and T. Rojac, "KNN-Based Piezoelectric Ceramics," pp. 81-102. in *Piezoelectric and Acoustic Materials for Transducer Applications*; Edited by A. Safari and E. K. Akdoğan. Springer US, Boston, MA, 2008.
14. G. Shirane, R. Newnham, and R. Pepinsky, "Dielectric Properties and Phase Transitions of  $\text{NaNbO}_3$  and  $(\text{Na,K})\text{NbO}_3$ ," *Phys. Rev.*, **96** [3] 581 (1954).
15. N. Raengthon, T. Sebastian, D. Cumming, I. M. Reaney, and D. P. Cann, " $\text{BaTiO}_3$ – $\text{Bi}(\text{Zn}_{1/2}\text{Ti}_{1/2})\text{O}_3$ – $\text{BiScO}_3$  Ceramics for High-Temperature Capacitor Applications," *J. Am. Ceram. Soc.*, **95** [11] 3554-61 (2012).
16. C. Stringer, R. Eitel, T. Shrout, C. Randall, and I. Reaney, "Phase Transition and Chemical Order in the Ferroelectric Perovskite  $(1-x)\text{Bi}(\text{Mg}_{3/4}\text{W}_{1/4})\text{O}_3$ – $x\text{PbTiO}_3$  Solid Solution System," *J. Appl. Phys.*, **97** [2] 4101 (2005).

17. R. E. Eitel, C. A. Randall, T. R. ShROUT, P. W. Rehrig, W. Hackenberger, and S.-E. Park, "New High Temperature Morphotropic Phase Boundary Piezoelectrics Based on  $\text{Bi}(\text{Me})\text{O}_3$ – $\text{PbTiO}_3$  Ceramics," *Jpn. J. Appl. Phys.*, **40** [10R] 5999-6002 (2001).
18. H. Ogihara, C. A. Randall, and S. Trolier - McKinstry, "High - Energy Density Capacitors Utilizing  $0.7\text{BaTiO}_3$ - $0.3\text{BiScO}_3$  Ceramics," *J. Am. Ceram. Soc.*, **92** [8] 1719-24 (2009).
19. B. Xiong, H. Hao, S. Zhang, H. Liu, and M. Cao, "Structure, Dielectric Properties and Temperature Stability of  $\text{BaTiO}_3$ – $\text{Bi}(\text{Mg}_{1/2}\text{Ti}_{1/2})\text{O}_3$  Perovskite Solid Solutions," *J. Am. Ceram. Soc.*, **94** [10] 3412-17 (2011).
20. L. E. Cross, "Relaxor Ferroelectrics," *Ferroelectrics*, **76** [1] 241-67 (1987).
21. I. Santos and J. Eiras, "Phenomenological Description of the Diffuse Phase Transition in Ferroelectrics," *J. Phys.: Condens. Matter*, **13** [50] 11733 (2001).
22. A. Bootchanont, N. Triamnak, S. Rujirawat, R. Yimnirun, D. P. Cann, R. Guo, and A. Bhalla, "Local Structure and Evolution of Relaxor Behavior in  $\text{BaTiO}_3$ – $\text{Bi}(\text{Zn}_{0.5}\text{Ti}_{0.5})\text{O}_3$  Ceramics," *Ceram. Int.*, **40** [9] 14555-62 (2014).
23. D. Viehland, S. Jang, L. E. Cross, and M. Wuttig, "Freezing of the Polarization Fluctuations in Lead Magnesium Niobate Relaxors," *J. Appl. Phys.*, **68** [6] 2916-21 (1990).
24. V. Shvartsman, J. Zhai, and W. Kleemann, "The Dielectric Relaxation in Solid Solutions  $\text{BaTi}_{1-x}\text{Zr}_x\text{O}_3$ ," *Ferroelectrics*, **379** [1] 77-85 (2009).
25. N. Raengthon, C. McCue, and D. P. Cann, "Relationship Between Tolerance Factor and Temperature Coefficient of Permittivity of Temperature-Stable High

- Permittivity BaTiO<sub>3</sub>-Bi(Me)O<sub>3</sub> Compounds," J. Adv. Dielectr., **6** [1] 1650002 (2016).
26. N. Raengthon, T. Sebastian, D. Cumming, I. M. Reaney, and D. P. Cann, "BaTiO<sub>3</sub>-Bi(Zn<sub>1/2</sub>Ti<sub>1/2</sub>)O<sub>3</sub>-BiScO<sub>3</sub> Ceramics for High - Temperature Capacitor Applications," J. Am. Ceram. Soc., **95** [11] 3554-61 (2012).
  27. N. Triamnak, R. Yimmirun, J. Pokorny, and D. P. Cann, "Relaxor Characteristics of the Phase Transformation in (1- x)BaTiO<sub>3</sub>-xBi(Zn<sub>1/2</sub>Ti<sub>1/2</sub>)O<sub>3</sub> Perovskite Ceramics," J. Am. Ceram. Soc., **96** [10] 3176-82 (2013).
  28. B. Jaffe, Chapters 5-7 in Piezoelectric Ceramics, Vol. 3. Elsevier, Amsterdam, Netherlands, 2012.
  29. G. Smolenskii and A. Agranovskaya, "Dielectric Polarization and Losses of Some Complex Compounds," Zh. Tekh. Fiz., **28** (1958).
  30. G. Samara and E. Venturini, "Ferroelectric/Relaxor Crossover in Compositionally Disordered Perovskites," Phase Transitions, **79** [1-2] 21-40 (2006).
  31. G. Smolenskii and V. Isupov, "Ferroelectric Properties of Solid Solutions of Barium Stannate in Barium Titanate)," Zh. Tekh. Fiz., **24** [8] 1375-86 (1954).
  32. A. Tagantsev and A. Glazounov, "Mechanism of Polarization Response in the Ergodic Phase of a Relaxor Ferroelectric," Phys. Rev. B, **57** [1] 18 (1998).
  33. T. R. Shrout and J. Fielding Jr, "Relaxor Ferroelectric Materials," pp. 711-20 in Ultrasonics Symposium, 1990. Proceedings., IEEE 1990.
  34. M. A. Akbas and P. K. Davies, "Processing and Characterization of Lead Magnesium Tantalate Ceramics," J. Mater. Res., **12** [10] 2617-22 (1997).

35. L. Farber and P. Davies, "Influence of Cation Order on the Dielectric Properties of  $\text{Pb}(\text{Mg}_{1/3}\text{Nb}_{2/3})\text{O}_3$ - $\text{Pb}(\text{Sc}_{1/2}\text{Nb}_{1/2})\text{O}_3$  (PMN - PSN) Relaxor Ferroelectrics," *J. Am. Ceram. Soc.*, **86** [11] 1861-66 (2003).
36. H. Ogihara, C. A. Randall, and S. Trolier - McKinstry, "Weakly Coupled Relaxor Behavior of  $\text{BaTiO}_3$ - $\text{BiScO}_3$  Ceramics," *J. Am. Ceram. Soc.*, **92** [1] 110-18 (2009).
37. G. H. Kwei, A. C. Lawson, S. J. L. Billinge, and S. W. Cheong, "Structures of the Ferroelectric Phases of Barium Titanate," *J. Phys. Chem.*, **97** 2368-77 (1993).
38. A. L. Hector and S. B. Wiggin, "Synthesis and Structural Study of Stoichiometric  $\text{BiTi}_2\text{O}_7$  Pyrochlore," *J. Solid State Chem.*, **177** [1] 139-45 (2004).
39. D. P. Shoemaker, R. Seshadri, A. L. Hector, A. Llobet, T. Proffen, and C. J. Fennie, "Atomic Displacements in the Charge Ice Pyrochlore  $\text{Bi}_2\text{Ti}_2\text{O}_6\text{O}'$  Studied by Neutron Total Scattering," *Phys. Rev. B*, **81** 144113 (2010).
40. D. P. Shoemaker, R. Seshadri, M. Tachibana, and A. L. Hector, "Incoherent Bi Off-Centering in  $\text{Bi}_2\text{Ti}_2\text{O}_6\text{O}'$  and  $\text{Bi}_2\text{Ru}_2\text{O}_6\text{O}'$ : Insulator versus Metal," *Phys. Rev. B*, **84** 064117 (2011).
41. E. Aksel, J. S. Forrester, J. C. Nino, K. Page, D. P. Shoemaker, and J. L. Jones, "Local Atomic Structure Deviation from Average Structure of  $\text{Na}_{0.5}\text{Bi}_{0.5}\text{TiO}_3$ : Combined X-Ray and Neutron Total Scattering Study," *Phys. Rev. B*, **87** 104113 (2013).
42. D. S. Keeble, E. R. Barney, D. A. Keen, M. G. Tucker, J. Kreisel, and P. A. Thomas, "Bifurcated Polarization Rotation in Bismuth-Based Piezoelectrics," *Adv. Funct. Mater.*, **23** 185-90 (2013).

43. V. A. Shuvaeva, D. Zekria, A. M. Glazer, Q. Jiang, S. M. Weber, P. Bhattacharya, and P. A. Thomas., "Local Structure of the Lead-Free Relaxor Ferroelectric  $(K_xNa_{1-x})(0.5)Bi_{0.5}TiO_3$ ," *Phys. Rev. B*, **71** 174114 (2005).
44. L. Liu, M. Knapp, H. Ehrenberg, L. Fang, L. A. Schmitt, H. Fuess, M. Hoetzel, and M. Hinterstein, "The Phase Diagram of  $K_{0.5}Na_{0.5}NbO_3$ - $Bi_{1/2}Na_{1/2}TiO_3$ ," *J. Appl. Crystallogr.*, **49** [2] 574-84 (2016).
45. T. M. Usher, J. S. Forrester, C. R. dela Cruz, and J. L. Jones, "Crystal Structure of  $0.96(Na_{0.5}Bi_{0.5}TiO_3)$ - $0.04(BaTiO_3)$  from Combined Refinement of X-Ray and Neutron Diffraction Patterns," *Appl. Phys. Lett.*, **101** 152906 (2012).
46. T.-M. Usher, I. Levin, J. E. Daniels, and J. L. Jones, "Electric-Field-Induced Local and Mesoscale Structural Changes in Polycrystalline Dielectrics and Ferroelectrics," *Sci. Rep.*, **5** 14678 (2015).
47. R. D. Shannon, "Revised Effective Ionic-Radii And Systematic Studies of Interatomic Distances in Halides and Chalcogenides," *Acta Crystallogr., Sect. A*, **32** [SEP1] 751-67 (1976).
48. A. Goaz, V. Uvarov, I. Popov, S. Shenawi-Khalil, and Y. Sasson, "A New Anhydrous Bismuth Potassium Nitrate,  $K_3Bi_2(NO_3)_9$ : Synthesis, Structure Characterization and Thermal Decomposition," *J. Alloys Compd.*, **514** 30-34 (2012).
49. Q. Zhang, Z. Li, F. Li, and Z. Xu, "Structural and Dielectric Properties of  $Bi(Mg_{1/2}Ti_{1/2})O_3$ - $BaTiO_3$  Lead-Free Ceramics," *J. Am. Ceram. Soc.*, **94** [12] 4335-39 (2011).

50. Y. Wang, X. Chen, H. Zhou, L. Fang, L. Liu, and H. Zhang, "Evolution of Phase Transformation Behavior and Dielectric Temperature Stability of BaTiO<sub>3</sub>-Bi(Zn<sub>0.5</sub>Zr<sub>0.5</sub>)O<sub>3</sub> ceramics system," *J. Alloys Compd.*, **551** 365-69 (2013).
51. X. Chen, J. Chen, D. Ma, L. Fang, and H. Zhou, "Thermally Stable BaTiO<sub>3</sub>-Bi(Mg<sub>2/3</sub>Nb<sub>1/3</sub>)O<sub>3</sub> Solid Solution with High Relative Permittivity in a Broad Temperature Usage Range," *J. Am. Ceram. Soc.*, **98** [3] 804-10 (2015).
52. A. Paterson, H. T. Wong, Z. Liu, W. Ren, and Z.-G. Ye, "Synthesis, Structure and Electric Properties of a New Lead-Free Ferroelectric Solid Solution of (1-x)BaTiO<sub>3</sub>-xBi(Zn<sub>2/3</sub>Nb<sub>1/3</sub>)O<sub>3</sub>," *Ceram. Int.*, **41** S57-S62 (2015).
53. H. Yu and Z.-G. Ye, "Dielectric Properties and Relaxor Behavior of a New (1-x)BaTiO<sub>3</sub>-xBiAlO<sub>3</sub> solid solution," *J. Appl. Phys.*, **103** 034114 (2008).
54. X. Huang, H. Hao, S. Zhang, H. Liu, W. Zhang, Q. Xu, and M. Cao, "Structure and Dielectric Properties of BaTiO<sub>3</sub>-BiYO<sub>3</sub> Perovskite Solid Solutions," *J. Am. Ceram. Soc.*, **97** [6] 1797-801 (2014).
55. X. Huang, H. Liu, H. Hao, Z. Wang, W. Hu, Q. Xu, L. Zhang, and M. Cao, "Structure, Dielectric and Impedance Properties of BaTiO<sub>3</sub>-Bi(Y<sub>0.5</sub>Yb<sub>0.5</sub>)O<sub>3</sub> Lead-Free Ceramics," *J. Mater. Sci.: Mater. Electron.*, **26** [5] 3215-22 (2015).
56. A. Zeb and S. J. Milne, "Temperature-Stable Dielectric Properties from -20° C to 430° C in the System BaTiO<sub>3</sub>-Bi(Mg<sub>0.5</sub>Zr<sub>0.5</sub>)O<sub>3</sub>," *J. Eur. Ceram. Soc.*, **34** [13] 3159-66 (2014).
57. Y. Wang, X. Chen, H. Zhou, L. Fang, L. Liu, and H. Zhang, "Evolution of Phase Transformation Behavior and Dielectric Temperature Stability of BaTiO<sub>3</sub>-Bi(Zn<sub>0.5</sub>Zr<sub>0.5</sub>)O<sub>3</sub> Ceramics System," *J. Alloys Compd.*, **551** 365-69 (2013).

58. A. Zeb and S. J. Milne, "Low Variation in Relative Permittivity over the Temperature Range 25–450 °C for Ceramics in the System  $(1-x)[\text{Ba}_{0.8}\text{Ca}_{0.2}\text{TiO}_3]-x[\text{Bi}(\text{Zn}_{0.5}\text{Ti}_{0.5})\text{O}_3]$ ," *J. Eur. Ceram. Soc.*, **34** [7] 1727-32 (2014).
59. X. Chen, J. Chen, G. Huang, D. Ma, L. Fang, and H. Zhou, "Relaxor Behavior and Dielectric Properties of  $\text{Bi}(\text{Zn}_{2/3}\text{Nb}_{1/3})\text{O}_3$ -Modified  $\text{BaTiO}_3$  Ceramics," *J. Electron. Mater.*, **44** [12] 4804-10 (2015).
60. A. Paterson, H. T. Wong, Z. Liu, W. Ren, and Z.-G. Ye, "Synthesis, Structure and Electric Properties of a New Lead-Free Ferroelectric Solid Solution of  $(1-x)\text{BaTiO}_3-x\text{Bi}(\text{Zn}_{2/3}\text{Nb}_{1/3})\text{O}_3$ ," *Ceram. Int.*, **41** Supplement 1 S57-S62 (2015).
61. H. Yu and Z.-G. Ye, "Dielectric Properties and Relaxor Behavior of a New  $(1-x)\text{BaTiO}_3-x\text{BiAlO}_3$  Solid Solution," *J. Appl. Phys.*, **103** [3] 4114 (2008).
62. V.M. Goldschmidt, "Die Gesetze der Krystallochemie," *Naturwissenschaften*, **14**[477] (1926).
63. M. R. Suchomel, A. M. Fogg, M. Allix, H. Niu, J. B. Claridge, and M. J. Rosseinsky, " $\text{Bi}_2\text{ZnTiO}_6$ : A Lead-Free Closed-Shell Polar Perovskite with a Calculated Ionic Polarization of  $150 \mu\text{C cm}^{-2}$ ," *Chem. Mater.*, **18** [21] 4987-89 (2006).
64. K. Miura, M. Kubota, M. Azuma, and H. Funakubo, "Electronic and Structural Properties of  $\text{BiZn}_{0.5}\text{Ti}_{0.5}\text{O}_3$ ," *Jpn. J. Appl. Phys.*, **48** [9S1] 09KF05 (2009).
65. D. D. Khalyavin, A. N. Salak, N. P. Vyshatko, A. B. Lopes, N. M. Olekhovich, A. V. Pushkarev, I. I. Maroz, and Y. V. Radyush, "Crystal Structure of Metastable Perovskite  $\text{Bi}(\text{Mg}_{1/2}\text{Ti}_{1/2})\text{O}_3$ : Bi-Based Structural Analogue of Antiferroelectric  $\text{PbZrO}_3$ ," *Chem. Mater.*, **18** [21] 5104-10 (2006).

66. M. Suewattana, D. J. Singh, and S. Limpijumnong, "Crystal Structure and Cation Off-Centering in  $\text{Bi}(\text{Mg}_{1/2}\text{Ti}_{1/2})\text{O}_3$ ," *Phys. Rev. B*, **86** [6] (2012).
67. V. Krayzman, I. Levin, J. C. Woicik, and F. Bridges, "Correlated Rattling-Ion Origins of Dielectric Properties in Reentrant Dipole Glasses  $\text{BaTiO}_3$ - $\text{BiScO}_3$ ," *Appl. Phys. Lett.*, **107** [19] 192903 (2015).
68. H. Takenaka, I. Grinberg, and A.M. Rappe, "Anisotropic Local Correlations and Dynamics in a Relaxor Ferroelectric," *Phys. Rev. Lett.*, **110**, 147602 (2013).
69. T.-M. Usher, "Local and Average Structures in Ferroelectrics under Perturbing Fields"; Ph.D Thesis, North Carolina State University, Raleigh, NC, 2016.
70. M. R. Suchomel, L. Ribaud, R. B. Von Dreele, and B. H. Toby, "Synchrotron Powder Diffraction Simplified: The High-Resolution Diffractometer 11-BM at the Advanced Photon Source," *Geochim. Cosmochim. Acta*, **74** [12] A1003-A03 (2010).
71. T. Proffen, T. Egami, S. J. L. Billinge, A. K. Cheetham, D. Louca, and J. B. Parise, "Building a High Resolution Total Scattering Powder Diffractometer Upgrade of NPD at MLNSC," *Appl. Phys. A*, **74** S163-S65 (2002).
72. P. F. Peterson, M. Gutmann, T. Proffen, and S. J. L. Billinge, "PDFgetN: A User-Friendly Program to Extract the Total Scattering Structure Factor and the Pair Distribution Function from Neutron Powder Diffraction Data," *J. Appl. Crystallogr.*, **33** 1192-92 (2000).
73. B. H. Toby, "EXPGUI, A Graphical User Interface for GSAS," *J. Appl. Crystallogr.*, **34** 210-13 (2001).



74. A. C. Larson and R. B. V. Dreele, "General Structure Analysis System (GSAS)." in Los Alamos National Laboratory Report LAUR 86-748. 2004.
75. C. L. Farrow, P. Juhas, J. W. Liu, D. Bryndin, E. S. Bozin, J. Bloch, T. Proffen, and S.J.L. Billinge, "PDFfit2 and PDFgui: Computer Programs for Studying Nanostructure in Crystals," *J. Phys.: Condens. Matter*, **19** 335219 (2007).
76. T. Egami and S. J. L. Billinge, *Underneath the Bragg Beaks: Structural Analysis of Complex Materials*; pp. 18. Pergamon: Kidlington, Oxford, UK, 2003.
77. D. H. Choi, A. Baker, M. Lanagan, S. Trolier - McKinstry, and C. Randall, "Structural and Dielectric Properties in  $(1-x)\text{BaTiO}_3-x\text{Bi}(\text{Mg}_{1/2}\text{Ti}_{1/2})\text{O}_3$  Ceramics ( $0.1 \leq x \leq 0.5$ ) and Potential for High - Voltage Multilayer Capacitors," *J. Am. Ceram. Soc.*, **96** [7] 2197-202 (2013).
78. G. L. Brenneka, H. J. Brown-Shaklee, M. A. Blea-Kirby, N. Raengthon, and D. P. Cann, "Capacitor Development for Reliable High Temperature Operation in Inverter Applications"; proceedings of the Electrical Energy Storage Applications and Technologies (EESAT) conference, San Diego, CA, December 1, 2013 (Paper No. SAND2013-10693C).
79. S. F. Wang and W. Huebner, "Interaction of Silver/Palladium Electrodes with Lead - and Bismuth - Based Electroceramics," *J. Am. Ceram. Soc.*, **76** [2] 474-80 (1993).
80. S. F. Wang and W. Huebner, "Interaction of Ag/Pd Metallization with Lead and Bismuth Oxide - Based Fluxes in Multilayer Ceramic Capacitors," *J. Am. Ceram. Soc.*, **75** [9] 2339-52 (1992).

81. N. Triamnak, G. L. Brenneka, H. J. Brown-Shaklee, M. A. Rodriguez, and D. P. Cann, "Phase Formation of  $\text{BaTiO}_3\text{-Bi}(\text{Zn}_{1/2}\text{Ti}_{1/2})\text{O}_3$  Perovskite Ceramics." *J. Ceram. Soc. Jpn.*, **122** [1424] 260-66 (2013).
82. A. Bokov and Z.-G. Ye, "Recent Progress in Relaxor Ferroelectrics with Perovskite Structure," pp. 31-52. in *Frontiers of Ferroelectricity*. Springer, Berlin, Germany, 2006.
83. A. J. Moulson and J. M. Herbert, *Electroceramics: Materials, Properties, Applications*. John Wiley & Sons, Hoboken, NJ, 2003.
84. N. Raengthon and D. P. Cann, "Dielectric Relaxation in  $\text{BaTiO}_3\text{-Bi}(\text{Zn}_{1/2}\text{Ti}_{1/2})\text{O}_3$  Ceramics," *J. Am. Ceram. Soc.*, **95** [5] 1604-12 (2012).
85. W. Jo, R. Dittmer, M. Acosta, J. Zang, C. Groh, E. Sapper, K. Wang, and J. Rödel, "Giant Electric-Field-Induced Strains in Lead-Free Ceramics for Actuator Applications—Status and Perspective," *J. Electroceram.*, **29** [1] 71-93 (2012).
86. V. V. Shvartsman and D. C. Lupascu, "Lead - Free Relaxor Ferroelectrics," *J. Am. Ceram. Soc.*, **95** [1] 1-26 (2012).
87. A. Glazounov and A. Tagantsev, "Direct Evidence for Vögel-Fulcher Freezing in Relaxor Ferroelectrics," *Appl. Phys. Lett.*, **73** 856 (1998).
88. M. A. Akbas and P. K. Davies, "Domain Growth in  $\text{Pb}(\text{Mg}_{1/3}\text{Ta}_{2/3})\text{O}_3$  Perovskite Relaxor Ferroelectric Oxides," *J. Am. Ceram. Soc.*, **80** [11] 2933-36 (1997).
89. R. Pirc and R. Blinc, "Spherical Random-Bond–Random-Field Model of Relaxor Ferroelectrics," *Phys. Rev. B*, **60** [19] 13470 (1999).

90. S. Bharadwaja, S. Trolier-McKinstry, L. Cross, and C. Randall, "Reentrant Dipole Glass Properties in  $(1-x)\text{BaTiO}_3-x\text{BiScO}_3$ ,  $0.1 \leq x \leq 0.4$ ," *Appl. Phys. Lett.*, **100** [2] 022906 (2012).
91. H. Y. Guo, C. Lei, and Z.-G. Ye, "Re-entrant Type Relaxor Behavior in  $(1-x)\text{BaTiO}_3-x\text{BiScO}_3$  Solid Solution," *Appl. Phys. Lett.*, **92** [17] 2901 (2008).
92. W. Kleemann, "The Relaxor Enigma—Charge Disorder and Random Fields in Ferroelectrics," pp. 129-36. in *Frontiers of Ferroelectricity*. Springer, Berlin, Germany, 2006.
93. G. A. Samara, "The Relaxational Properties of Compositionally Disordered  $\text{ABO}_3$  Perovskites," *J. Phys.: Condens. Matter*, **15** [9] R367 (2003).
94. N. Kumar, A. Ionin, T. Ansell, S. Kwon, W. Hackenberger, and D. P. Cann, "Multilayer Ceramic Capacitors Based on Relaxor  $\text{BaTiO}_3\text{-Bi}(\text{Zn}_{1/2}\text{Ti}_{1/2})\text{O}_3$  for Temperature Stable and High Energy Density Capacitor Applications," *Appl. Phys. Lett.*, **106** [25] 252901 (2015).
95. N. Kumar and D. P. Cann, "Resistivity Enhancement and Transport Mechanisms in  $(1-x)\text{BaTiO}_3-x\text{Bi}(\text{Zn}_{1/2}\text{Ti}_{1/2})\text{O}_3$  and  $(1-x)\text{SrTiO}_3-x\text{Bi}(\text{Zn}_{1/2}\text{Ti}_{1/2})\text{O}_3$ ," *J. Am. Ceram. Soc.*, **98** [8] 2548-55 (2015).
96. N. Raengthon, V. J. DeRose, G. L. Brennecke, and D. P. Cann, "Defect Mechanisms in High Resistivity  $\text{BaTiO}_3\text{-Bi}(\text{Zn}_{1/2}\text{Ti}_{1/2})\text{O}_3$  Ceramics," *Appl. Phys. Lett.*, **101** [11] 112904 (2012).
97. N. Kumar, E. A. Patterson, T. Frömling, and D. P. Cann, "DC-Bias Dependent Impedance Spectroscopy of  $\text{BaTiO}_3\text{-Bi}(\text{Zn}_{1/2}\text{Ti}_{1/2})\text{O}_3$  Ceramics," *J. Mater. Chem. C*, **4** [9] 1782-86 (2016).

98. D. M. Smyth, *The Defect Chemistry of Metal Oxides*. Oxford University Press, Oxford, UK, 2000.
99. A. Müller and K. Härdtl, "Ambipolar Diffusion Phenomena in BaTiO<sub>3</sub> and SrTiO<sub>3</sub>," *Appl. Phys. A*, **49** [1] 75-82 (1989).
100. M. Li, M. J. Pietrowski, R. A. De Souza, H. Zhang, I. M. Reaney, S. N. Cook, J. A. Kilner, and D. C. Sinclair, "A Family of Oxide Ion Conductors Based on the Ferroelectric Perovskite Na<sub>0.5</sub>Bi<sub>0.5</sub>TiO<sub>3</sub>," *Nat. Mater.*, **13** [1] 31-35 (2014).
101. N. Kumar, E. A. Patterson, T. Frömling, and D. P. Cann, "Conduction Mechanisms in BaTiO<sub>3</sub>-Bi(Zn<sub>1/2</sub>Ti<sub>1/2</sub>)O<sub>3</sub> Ceramics," Submitted to *J. Am. Ceram. Soc.* (Manuscript under revision), (2016).
102. N. H. Chan and D. Smyth, "Defect Chemistry of BaTiO<sub>3</sub>," *J. Electrochem. Soc.*, **123** [10] 1584-85 (1976).
103. Y. Tsur and C. A. Randall, "Point Defect Concentrations in Barium Titanate Revisited," *J. Am. Ceram. Soc.*, **84** [9] 2147-49 (2001).
104. R. Moos and K. H. Härdtl, "Dependence of the Intrinsic Conductivity Minimum of SrTiO<sub>3</sub> Ceramics on the Sintering Atmosphere," *J. Am. Ceram. Soc.*, **78** [9] 2569-71 (1995).
105. N. H. Chan and D. M. Smyth, "Defect Chemistry of Donor - Doped BaTiO<sub>3</sub>," *J. Am. Ceram. Soc.*, **67** [4] 285-88 (1984).
106. N. Kumar and D. P. Cann, "Tailoring Transport Properties through Non-Stoichiometry in BaTiO<sub>3</sub>-BiScO<sub>3</sub> and SrTiO<sub>3</sub>-Bi(Zn<sub>1/2</sub>Ti<sub>1/2</sub>)O<sub>3</sub> for Capacitor Applications," *J. Mater. Sci.* **51** 9404 (2016).

## Figure Captions

**Figure 1.** (a) Temperature-dependent relative permittivity for a variety of compositions in the (1-x)BT-xBZT system, (b) relative permittivity versus temperature for 0.93BT-0.07BZT as a function of frequency, demonstrating moderate DPT behavior, and (c) temperature-dependent relative permittivity for 0.89BT-0.11BZT, demonstrating relaxor characteristics (from Triamnak et al.<sup>27</sup>, used with permission).

**Figure 2.** Relative permittivity versus temperature for 0.50BaTiO<sub>3</sub>-0.25BiZn<sub>1/2</sub>Ti<sub>1/2</sub>O<sub>3</sub> - 0.25BiScO<sub>3</sub>. For comparison, the inset shows typical temperature dependence of permittivity for relaxor PbMg<sub>1/3</sub>Nb<sub>2/3</sub>O<sub>3</sub> and normal ferroelectric BaTiO<sub>3</sub> (inset is adapted from Shrout and Fielding<sup>33</sup>).

**Figure 3.** Relative permittivity as a function of applied electric field (dc) bias at room temperature for several commercial capacitors including BaTiO<sub>3</sub>-based Y5V and X7R, PbNb<sub>0.024</sub>Zr<sub>0.517</sub>Ti<sub>0.459</sub>O<sub>3</sub>, commercial CaZrO<sub>3</sub>-based NP0, and 0.8BaTiO<sub>3</sub>-0.2BiZn<sub>1/2</sub>Ti<sub>1/2</sub>O<sub>3</sub>.

**Figure 4.** Temperature-dependent resistivity and associated activation energies for charge transport measured for commercial BaTiO<sub>3</sub>-based X7R and Y5V capacitors, as well as PZT-5a, and 0.8BaTiO<sub>3</sub>-0.2BiZn<sub>1/2</sub>Ti<sub>1/2</sub>O<sub>3</sub> pellet samples.

**Figure 5.** (a) Representative qualitative phase diagram for  $\text{BaTiO}_3 - \text{Bi(M)O}_3$  systems. The phase boundary between the high-temperature cubic phase and the lower-temperature pseudocubic phase is currently undetermined and the slope likely varies with different  $\text{M}^{3+}$  cations (data extracted from <sup>36,49,54,56-61</sup>). (b) Compositional limit (between  $\text{P4mm}$  and pseudocubic phase) for  $\text{BaTiO}_3 - \text{Bi(M)O}_3$  systems as a function of tolerance factor of  $\text{Bi(M)O}_3$ . Error bars report the compositional range within which the phase boundary lies.

**Figure 6.** Discrete datapoints (red x) are X-ray diffraction (top panel) and neutron diffraction (bottom panel) patterns of 0.94BT-0.06BZT. Modeled data (continuous lines) are the best fit model produced from a combined Rietveld refinement of both X-ray and neutron data using a combination of  $\text{P4mm}$  and  $\text{Pm}\bar{3}\text{m}$  space groups. The difference pattern and hkl markers are shown below each pattern. The insets show magnified views of select characteristic reflections.

**Figure 7.** X-ray diffraction (top panel) and neutron diffraction (bottom panel) patterns (red x). A model is refined using both datasets in a Rietveld refinement of 0.8BT-0.2BZT using the  $\text{P4mm}$  space group. The refined model is shown as a continuous line, along with the difference pattern and hkl markers below each plot. The insets show magnified views of select characteristic reflections.

**Figure 8.** Pair distribution functions of 0.8BT-0.2BZT. The data within individual 10 Å ranges are separately fit (box car fitting), demonstrating that the best fit to individual ranges results in a decreasing  $c/a$  ratio with increasing atom-atom distances.

**Figure 9.** Box-car analysis of the PDFs result in lattice parameters as a function of length scale, shown in this figure as red and black symbols. The blue lines indicate the tetragonal lattice parameters obtained from the Rietveld refinements and the dashed pink line represents the lattice parameter for the cubic phase obtained from the Rietveld refinements. Error bars are smaller than the symbols.

**Figure 10.** Ellingham diagram showing the thermodynamic equilibrium conditions for oxidation / reduction of several species of interest for BT-Bi(M)O<sub>3</sub>-based capacitors. The melting point of metallic Cu is also indicated.

**Figure 11.** In situ RGA data showing the gas evolution and temperature rise associated with MLCC binder burnout. An exothermic rise in temperature detectable at ~160 °C agrees well with combustion products.

**Figure 12.** Even after complete binder removal was verified by RGA, 0.8BT-0.2BZT dielectrics cofired with Pt electrodes at 1200 °C in flowing O<sub>2</sub> and intended for use as high voltage capacitors exhibited catastrophic delamination (a) and bubbling (b).

**Figure 13.** In situ RGA oxygen signal collected during MLCC sintering. A modest increase in both molecular oxygen (32 atomic mass units) and atomic oxygen (16 atomic mass units) signals initiates at 1020 °C

**Figure 14.** 0.80BT-0.20BZT sintered at 1000 °C produced MLCCs that (a) were relatively dense (~95 %), experienced little or no interaction with the Pt electrode, and (b) exhibited similar dielectric properties to ceramic discs sintered to full density at 1120 °C. (c) The MLCC is shown with a U.S. dime for scale.

**Figure 15.** (a) In situ hot stage XRD of 0.8BT-0.2BZT during solid state reaction of precursors, with two isothermal holds at 980 and 1120 °C to mimic typical calcination and sintering steps; (b) zoomed-in view of the (110) reflection peak during the isothermal hold at 1120 °C; (c) two individual scans taken at the beginning and the end of the 1120 °C isotherm.

**Figure 16.** Proposed mechanism for reaction pathways of BT-BZT from typical precursors; (a) unreacted precursor powders BaCO<sub>3</sub> (blue), Bi<sub>2</sub>O<sub>3</sub> (yellow), and TiO<sub>2</sub> (red); (b) precursors react to form the first intermediate phase BaBi<sub>4</sub>Ti<sub>4</sub>O<sub>15</sub> (BBT, gray); (c) intermediate phase BaBiO<sub>3</sub> forms at higher temperatures; (d) at temperatures near 900 °C, the remaining Bi<sub>2</sub>O<sub>3</sub> reacts to form the intermediate phase Bi<sub>4</sub>Ti<sub>3</sub>O<sub>12</sub> (BiT, purple) and the perovskite solid solution BT-BZT (BT(SS), green); (e) further heating leads to consumption of all intermediate phases except BiT; (f) after holding at the calcination temperature, all that remains is single-phase BT-BZT (BT(SS)).



**Figure 17.** (a) Optical photograph of one type of powder discoloration effect frequently observed after calcination of BT-BZT (and related) powders. (b) XRF measurements suggest that discoloration may be related to Bi diffusion, but chemical analysis (via XRF and other techniques—see text) is inconclusive.

**Figure 18.** (a) Polished surfaces of BT-BZT ceramics (here, 0.8BT-0.2BZT) after thermal etching reveal dense and seemingly homogeneous microstructures, but (b) highly-contrasted backscatter images of the same materials reveal evidence of chemical heterogeneity within the grains.

**Figure 19.** TEM-EDS composition maps showing that the contrast from Figure 18 correlates with small variations in Ba / Bi distribution within the 0.8BT-0.2BZT grains.

**Figure 20.** Independent TEM-EDS scans on 0.8BT-0.2BZT samples fabricated in a different lab confirmed the presence and levels of cation heterogeneity.

**Figure 21.** Representative highly contrasted backscatter SEM images of effectively (a) donor-doped and (b) acceptor-doped 0.8BT-0.2BZT ceramics showing the effects of doping (via control of cation mobility) on microstructure and chemical heterogeneity.

**Figure 22.** Relative permittivity as a function of temperature for (a) BT-BZT-based ceramics (from Raengthon et al.<sup>26</sup>, used with permission), (b) 0.7BT-0.3BS (from

Ogihara et al.<sup>18</sup>, used with permission), (c) BaTiO<sub>3</sub>-Bi(Ni<sub>1/2</sub>Ti<sub>1/2</sub>)O<sub>3</sub> (BT-BNiT) (from Kumar and Cann<sup>83</sup>, used with permission), and (d) a representative canonical relaxor (adapted from Bokov and Ye<sup>82</sup>). The BI stands for BiInO<sub>3</sub>, NR for non-ergodic, ER for ergodic, PE for paraelectric, CW for Curie-Weiss, URD for universal relaxation dispersion, CRD for conventional relaxation dispersion, and T<sub>f</sub>, T<sub>B</sub> and T<sub>m</sub> are freezing temperature, Burns temperatures and temperature of maximum permittivity (T<sub>max</sub>) respectively. The CRD and URD are empirical contributions to relative permittivity based on their frequency response and both are related to relaxation-type polarizations. While the real and imaginary parts of URD decrease with frequency ( $\propto f^{n-1}$ , where f is frequency and n lies between 0 and 1), the real part of CRD is constant at small enough frequencies and approaches a value of zero as frequency approaches a characteristic value.

**Figure 23.** Re-entrant behavior shown in xBT-(1-x)BS ceramics using switchable polarization measured at different electric fields as a function of temperature (from Bharadwaja et al.<sup>90</sup>, used with permission).

**Figure 24.** (a) Polarization-electric field loop for 0.7BT-0.3BS with the area representing energy density highlighted in blue (from Ogihara et al.<sup>18</sup>, used with permission), (b) energy density of 0.7BT-0.3BS as compared with some commercial MLCCs (adapted from Viehland et al.<sup>23</sup>), and (c) energy density of 0.85BT-0.15BZT MLCCs as a function of temperature (from Kumar et al.<sup>94</sup>, used with permission).

**Figure 25.** Arrhenius plots of bulk resistivity values measured in air using ac impedance spectroscopy for (a) BT-BZT ceramics, (b) ST-BZT ceramics, and (c) BT-BS and BT-BNiT ceramics. The bulk resistivity values of BaTiO<sub>3</sub> and SrTiO<sub>3</sub> have also been shown for reference (from Kumar et al.<sup>95</sup>, used with permission).

**Figure 26.** (a) Nyquist plots for BT with ac impedance spectroscopy performed in vacuum, air and oxygen (from Kumar et al.<sup>101</sup>, used with permission). The inset shows the zoomed-in version of high-frequency arcs of bulk resistivity. (b) Defect diagram for undoped or p-type doped BT (adapted from Smyth<sup>98</sup>). The  $n$  is electron concentration and  $A'$  represents an acceptor dopant.

**Figure 27.** (a) Nyquist plots for stoichiometric 0.97BT-0.03BZT with ac impedance spectroscopy performed in vacuum, air and oxygen. (b) Nyquist plots for stoichiometric 0.95ST-0.05BZT with ac impedance spectroscopy performed in nitrogen, air and oxygen. (c) Nyquist plots for stoichiometric 0.97BT-0.3BS with ac impedance spectroscopy performed in nitrogen, air and oxygen (from Kumar, et al.<sup>101,106</sup>, used with permission).

**Figure 28.** Seebeck measurements on BT and 0.97BT-0.03BZT ceramics exhibiting p-type and n-type behavior respectively.

**Figure 29.** Electrical conductivities at 1000 °C as a function of  $pO_2$  for BT doped with various amounts of Al and Nb (from Chan and Smyth,<sup>105</sup> used with permission).

**Figure 30.** Arrhenius plots of bulk resistivity in air as obtained from ac impedance spectroscopy for (a) stoichiometric (S) and non-stoichiometric (Bi excess, Sr deficient, Sr excess) 0.95ST-0.05BZT, (b) stoichiometric (S) and Ba-deficient (-2Ba) 0.8BT-0.2BZT, and (c) stoichiometric (S) and non-stoichiometric (Bi excess, Ba deficient, Bi deficient) 0.7BT-0.3BS (from Raengthon, et al.<sup>96</sup> and Kumar and Cann,<sup>106</sup> used with permission)